Rosen, David L.

PICOSECOND AND STEADY STATE SPECTROSCOPY OF DEFECTS IN SEMI-INSULATING CADMIUM-SELENIDE

City University of New York PH.D. 1985

PICOSECOND AND STEADY STATE SPECTROSCOPY OF DEFECTS IN SEMI-INSULATING CdSe

by

David L. Rosen

A dissertation submitted to the Graduate Faculty in Physics in partial fulfillment of the requirements for the degree of Doctor of Philosophy, the City University of New York.

1985

This manuscript has been read and accepted for the Graduate Faculty in Physics in satisfaction of the dissertation requirement for the degree of Doctor of Philosophy.

9/30/85
date

Chairman of Examining Committee

9/4/85
date

Executive Officer

Supervisory Committee

The City University of New York

ABSTRACT

by David L. Rosen

Advisor: Professor R. R. Alfano

The goal of this thesis was to understand how defects control the dynamics of electrons in a semiconductor under optical excitation. Time resolved and steady state spectroscopy showed that defects determine the optical and electrical properties of undoped, semi-insulating(SI) CdSe. Nonlinear photoluminescence, picosecond recombination, induced dichroism, the Kerr effect and two step absorption were measured. The important physics in this work was characterizing the three defect bands that cause these effects in SI CdSe. First, the main recombination center is a deep donor(R), ≈1.3 eV above the valence band, with very large cross sections for free carrier capture. This level R has degenerate levels, as shown by the induced dichroism. Second, a shallow acceptor(A), 105 meV above the valence band, is also a recombination center. Third, a conduction band tail(T), consisting of shallow donors, is a luminescence center. Comparisons between undoped low resistivity CdSe and SI CdSe suggest these levels also cause the high resistivity properties of SI CdSe. A two level model by Klasens, using both R and A, explains the nonlinear photoluminescence under low intensity, steady state excitation. Models, using these defect levels, were constructed that explain the picosecond results. The methods and theories developed in this thesis could be used in the quality control and fabrication of semiconductor devices.

ACKNOWLEDGEMENTS

I sincerely thank many people who have given me help and advice. My biggest debt is to my parents, whose sacrifice and love carried me through this most difficult period. I especially thank my research advisor Prof. R. R. Alfano, who gave me the opportunity and guidance to work with both picosecond technology and semiconductor physics. I thank Mr. Q. X. Li for helping me with my measurements. I thank Prof. Neumark, Prof. Lax and Prof. Birman for their helpful discussions of semiconductor theory. I thank Prof. Gersten for helping me with the computer programming. I thank Megan Gibbs for typing and technical aid. Dr. Ockman, Ms. Foresti and Dr. Zarrabi were helpful in providing measurements that strengthened this work. I could not finish this thesis without help from the entire IUSL team. Most of all, I thank the Air Force Office for Scientific Research for supporting this research. I finally thank Janet Weissman, David Harris and Jeannette Wolffe, friends who put everything in perspective.

TABLE OF CONTENTS

LIST OF TABLES

LIST OF FIGURES

Chapter 1 Introduction

Chapter 2 Steady State Investigation

Chapter 3 Picosecond Absorption and Polarization

Chapter 1

Introduction

1.1 DEFECTS IN SOLIDS

In solid state physics, one is first introduced to the concept of an ideal crystal with no unintentional chemical impurities or native atoms out of place. All impurities present are intentionally added dopants, and all dopants are either hydrogenic donors or hydrogenic acceptors. Although such a model is useful for predicting and understanding general properties of crystals, these crystals are only grown in textbooks. In actual crystals there are always unintentional defects and deep levels(Bourgoin and Lanoo,1983; Newmark and Kosa,1983). It is now known that in actual fact, most of the interesting properties of crystals are not determined so much by the properties of the perfect crystal(intrinsic properties) as by its imperfections(extrinsic properties). Both misplaced atoms(native defects) and chemical impurities are called defects.

The study of semiconductor defects is an active scientific field. The existence of the semiconductor industry is based on the ability to control the electrical conductivity of semiconductors by trace additions of shallow donor and acceptor chemical impurities. Display phosphors are usually large bandgap semiconductors with trace luminescence centers added. Uncontrollable deep levels from growth, radiation damage and device usage degrade device performance. Future applications of semiconductors in electrical and optical devices will require the measurement and understanding of

semiconductor defects.

Most standard methods of measuring and detecting defects are not sensitive enough to measure the small defect concentrations($<10^{16}cm^{-3}$), which are much smaller than the concentration of intrinsic atoms($3.6x10^{22}cm^{-3}$ in CdSe). As such small quantities are also hard to control, large variations between samples are unavoidable. Even when the defects are chemically or physically known, the properties these defects are changing may not be known(Stringfellow and Bube, 1968).

Optical spectroscopic techniques are useful because they are very sensitive to small defect concentrations and because they are nondestructive. Although optical measurements often do not reveal the chemical or physical nature of the defects, they can be used to model many optical and electrical properties that are important in technology. An example is the EL2 defect in GaAs, which is optically monitored in the manufacture of semi-insulating(SI) GaAs even though its chemical nature is still not certain(Sturge,1962; Mitonneau and Mircea,1979; Martin,1981). Optical measurements are thus useful in both semiconductor characterization and fundamental experiments. This thesis project studied defects in undoped CdSe using optical spectroscopy. Many of the measurements were on a picosecond time scale. Picosecond spectroscopy is well known to be sensitive to crystal defects and quality(Auston et. al., 1972; Huppert et. al., 1972; von der Linde et. al.,1974). However, there are few complete studies, using picosecond techniques, of defects in semiconductors.

1.2 RECOMBINATION THROUGH DEFECT LEVELS

Free carrier recombination and internal transitions of defect levels are studied in this thesis. A defect level can capture or emit an electron in the conduction band, the valence band or another defect level. Both the energy difference and the momentum difference between the defect level and the other electron must be absorbed by a third excitation. This third excitation is usually either a photon, another free carrier, an optical phonon or an acoustical phonon. These four types of processes are respectively called radiative transition, Auger processes, multiphonon emission(MPE) and the cascade mechanism(Bourgoin and Lanoo,1983; Neumark and Kosa,1983). These processes will be physically described in terms of energy and momentum transfer. In the schematics of this thesis, straight vertical lines indicate radiative transitions, during which photons are emitted or absorbed, and wavy vertical lines indicate nonradiative transitions, during which only phonons are emitted or absorbed. The cascade mechanism will be shown, in chapter 3, to be active in CdSe.

In radiative transition, when an electron or hole is captured or emitted, the excess energy is emitted or absorbed by a photon. A high energy photon has a much larger momentum than most thermal electrons, so a radiative transition is not as probable as other transitions. However, the photon emitted or absorbed is easily detected as luminescence or by optical absorption.

In Auger processes, when an electron and a hole recombines near another free carrier or defect, the excess energy is absorbed by the third particle. Auger with a third free carrier instead of a defect is called band-to-band Auger. Band-to-band Auger is shown in figure 1.2.1. In band-to-band Auger, the larger the energy bandgap, the more kinetic energy and the more momentum the remaining free carrier gains. Because of conservation of momentum, band-to-band Auger is unlikely in large bandgap semiconductors such as CdSe(Landsberg and Beattie,1959; Neumark,1973). When a defect, instead of a third free carrier, carries away the excess energy, the Auger process is enhanced. This process is shown in figure 1.2.2. The rate of photoexcited carrier decay caused by an Auger process is excitation intensity dependent and non-exponential because of the participation of two or three carriers.

In multiphonon emission(MPE), an electron or hole captured by a defect level emits optical phonons(Neumark and Kosa,1983; Bourgoin and Lannoo,1983), as shown in figure 1.2.3. The electron transfers down a series of vibrational levels of the defect, emitting an optical phonon at each step. An optical phonon can have a large energy and a small momentum, so MPE is usually much faster than Auger or radiative processes. Because ambient optical phonons increase the rate of phonon emission, the rate of MPE increases with increasing temperature. The MPE rate, w, obeys the following equation for free carrier capture at high temperatures:

$$w=w_0 T^{0.5}\exp(-E_b/k_B T) \qquad (1.2.1)$$

where w_o is a constant, and E_b is the activation energy(which is approximately the binding energy of the defect level). This formula is valid if the thermal energy(k_BT) is greater than the optical phonon energy.

In the cascade mechanism, an electron makes a transition between levels by emitting acoustical phonons(Lax,1959; Henry and Lang,1977; Abram,1982). The capture of an electron by a cascade mechanism is shown in figure 1.2.4. The cascade process can only occur between two widely spaced energy levels if a series of electronic levels exists between them, in contrast to MPE which requires only a series of vibrational levels. In a cascade transition, the electron transfers down this ladder of electronic states, emitting an acoustical phonon at each step. Because an acoustical phonon carries more momentum than an optical phonon, each step must be very small in energy. A large momentum acoustical phonon can also be absorbed, moving an electron up this ladder. The cascade capture rate decreases with increasing temperature, because ambient, large momentum phonons are absorbed at high temperatures. When this ladder of electronic levels exists, the cascade process is often much faster than the MPE process because each step requires a smaller amount of energy in cascade than in MPE.

This thesis will focus on the special case of a cascade transition between two defect levels, as shown in figure 1.2.5. Consider two localized energy levels E_1 and E_2, with a series of electronic levels $E(r_o)$ between them. An electron in level $E(r_o)$ has an orbital radius r_o which is determined by the momentum of

the thermal phonon previously emitted. An electron, with a mean free path L, makes a cascade transition from E_1 to E_2. The rate, w, of the first step from E_1 to the initial $E(r_o)$ is given by(Lax,1959):

$$w \sim r_o^2 L^{-1} E(r_o) E_1^{-1} \tag{1.2.2}$$

If the temperature is T, $L \sim T^{-1}$, $E(r_o) \sim T^2$ and $r_o \sim T^{-2}$ and E_1 is independent of T, so that:

$$w \sim T^{-3} \tag{1.2.3}$$

This special case differs from the capture of a thermal free carrier where $E_1 \sim T$. In chapter 3, defect level to defect level cascade transition will be used to explain the experimental results.

It should be noted that more than one mechanism can occur simultaneously in a transition. Auger, MPE and cascade transitions can simultaneously occur between two levels. Several of these processes may also occur in series. For example, if the ladder of states required in the cascade process does not extend entirely from E_1 to E_2, the electron could make a transition by cascade down the ladder and release the rest of the energy by either Auger or MPE. In this situation, the temperature dependence of the transition rate depends on the slowest(i.e., rate determining) step.

1.3 CADMIUM SELENIDE

The semiconductor studied in this thesis was cadmium selenide(CdSe), for the following five reasons. First, it has a fairly large bandgap(1.73 eV-1.83 eV), which makes it useful in certain opto-electronic applications. It is currently used for high power IR retarders and parametric generators, and it has potential applications in solar power, photodetectors and light emitting diodes. Second, its nonlinear and excitonic properties have been extensively studied(Kuroda and Shionoya, 1981; Shah, 1974). Third, it has a wurtzite structure(symmetry group C_{6v}), with an optical axis, so that the polarization of the luminescence from impurities could be studied. Fourth, it can be easily made semi-insulating. Fifth, CdSe has a property called self-compensation(i.e., it is naturally n-type). Semi-insulation and self-compensation, which will now be described, are two interesting properties of some semiconductors.

This thesis will concentrate on undoped, semi-insulating(SI) CdSe. Semi-insulating crystals are semiconductor crystals which have an electrical resistivity $>10^6$ Ω-cm, as compared with the usual semiconductor resistivity <20 Ω-cm. Undoped CdSe crystals, after growth, are generally cadmium rich with an n-type resistivity ≈10 Ω-cm. In order to raise its resistivity, a CdSe crystal is often heated in Se vapor(i.e., Se-annealed) which both adds Se to the crystal and makes it a stoichiometric, high resistivity crystal $>10^8$ Ω-cm(Heinz and Banks,1956; Hung et. al.,1969; Ture et. al.,1983). The annealed material is called undoped, SI

CdSe because the added Se is not considered a chemical impurity. Undoped, SI CdSe is often confused with intrinsic(i.e., ultrahigh purity) CdSe although it is probably only compensated(i.e., a large but balanced mixture of impurities). Undoped, SI CdSe is very similiar to undoped SI GaAs, which is made by annealing GaAs in As vapor and is a very important material in microwave technology and high speed electronics. In addition to Se-vapor annealing, SI CdSe can also be made by adding shallow acceptor impurities.

Self-compensation is a property where a semiconductor either resists p-doping(such as CdSe and ZnSe), resists n-doping(such as Cu_2O or GaSe) or resists all doping(such as ZnS). As the wrong type of dopant is added, the electrical resistance of the crystal increases. For example, if shallow acceptor impurities are added to CdSe, it becomes SI CdSe, so there is no low resistivity p-type CdSe. Self-compensation is a property of many large bandgap semiconductors. The use of large bandgap semiconductors in technology is largely impeded by the self-compensation effect, because it prevents the fabrication of p-n junctions from these semiconductors. One important potential application of large bandgap semiconductors, using p-n junctions, is visible semiconductor lasers.

In self-compensation, adding the wrong type of shallow dopant increases the concentration of deep level defects, which increases the electrical resistivity of the crystal. Three possible mechanisms for self-compensation are the chemical generation of deep level defects when the shallow acceptor is added, the selective solubility of impurities from the environment of the

crystal melt, and dopants which contain both shallow levels and deep levels(Mandel,1964; Longini and Greene,1956; Kobayashi et. al.,1983). The self-compensation mechanism for CdSe is not completely known. For this reason, this thesis started with studies of the shallow acceptor in SI CdSe.

Defects in CdSe have been studied by electrical measurement techniques such as deep level transient spectroscopy(DLTS), optical DLTS(ODLTS), photoconductivity(PC) and photo-Hall(PH) measurements(Ture et. al.,1983; Bube et. al.,1961; Fowler,1961). However, SI CdSe is usually not studied by DLTS because of problems involving the high resistance, non-Ohmic contacts and low resistance surface layers. However, partially annealed samples of CdSe(1 Ω-cm<ρ<100 Ω-cm) have been studied by DLTS and ODLTS. Three deep acceptors(0.6, 0.7 and 0.15 eV above the valence band) and a deep donor(0.12 eV below the conduction band) were shown by DLTS and ODLTS. Deep acceptors are shown in the PL(≈0.9 μm) and PC of SI CdSe(Belen'kii et. al.,1968). However, these levels do not explain the data of the SI samples (ρ>10^8 Ω-cm) described in this thesis. Nanosecond PC has shown that two defect levels dominate the recombination in undoped, SI CdSe, although the energy of these levels are unknown(Vaitkus and Vishchakas,1968).

Six types of experiments were done on undoped, Se-vapor annealed SI CdSe in this thesis. First, the steady state photoluminescence(PL) spectrum was studied as a function of excitation intensity in order to identify recombination pathways. Second, steady state absorption was used to verify the existence of a deep level in undoped, SI CdSe. Third, pump-probe absorption studies

were done to time resolve the defect level transition rates. Fourth, pump-probe polarization studies found degenerate states in the deep level and measured transition rates between them. Fifth, intense pulse transmission and time integrated anti-Stokes PL proved the existence of two step absorption into the conduction band. Sixth, picosecond PL was measured by streak camera to prove that defects capture free carriers on a picosecond time scale.

The important physics in this work was characterizing three defect bands and showing how these bands influence many of the optical and electrical properties of undoped SI CdSe. The three bands are the deep donor, the shallow acceptor and the shallow donors. These defects were not intentionally added to the crystal, and the physical and chemical nature of these defect levels could not be found using these optical techniques. However, the properties that were studied do not require a full understanding of the chemical nature of these defects. The methods and theories used in this thesis could be applied to any semiconductor, even inside a device component. Therefore, these techniques could be used in the quality control of semiconductor devices.

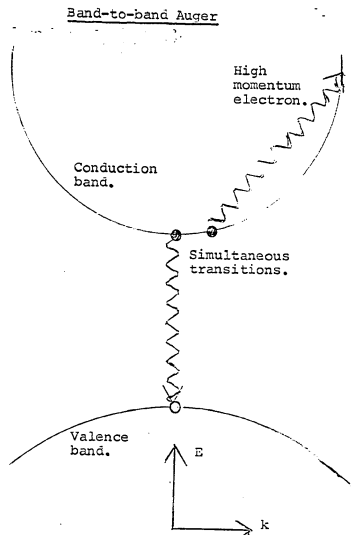

Fig. 1.2.1: Band-to-band Auger. An electron-hole pair recombines, while another free carrier(shown here as an electron) gains both energy, E, and momentum, k. This process is unlikely, in large band-gap semiconductors, by conservation of momentum.

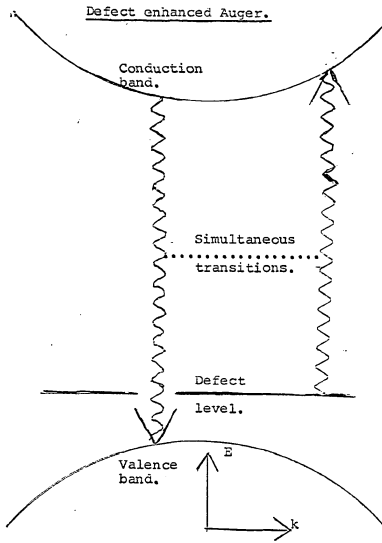

Fig. 1.2.2: Defect enhanced Auger. An electron-hole pair recombines, while a free carrier(here shown as a conduction electron) is emitted from a defect level. Because the remaining free carrier has a small kinetic energy and a small momentum, this process is more probable than band-to-band Auger.

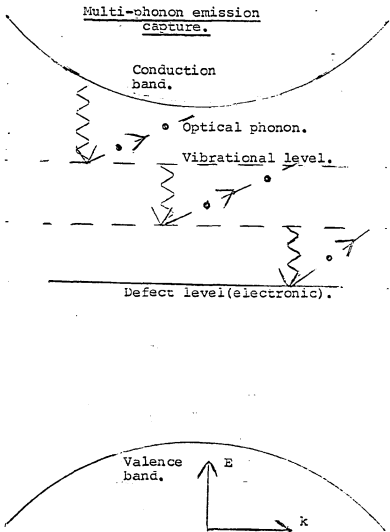

Fig. 1.2.3: Multiphonon emission capture. A free carrier(shown as an electron) is captured by a defect by emmitting optical phonons. The only intermediate levels are vibrational levels of the defect. The capture rate increases with temperature.

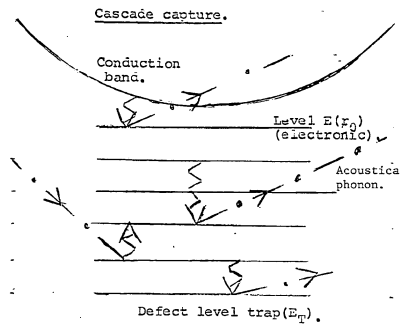

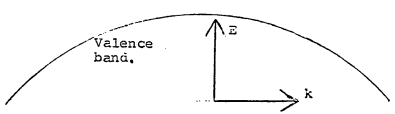

Fig. 1.2.4: Cascade capture. Defect level, E_T, captures a free carrier by emitting acoustical phonons. The free carrier makes intermediate transitions down a ladder of electronic levels, $E(r_0)$, of the defect. The capture rate into E_T decreases with temperature due to absorption of ambient, acoustical phonons.

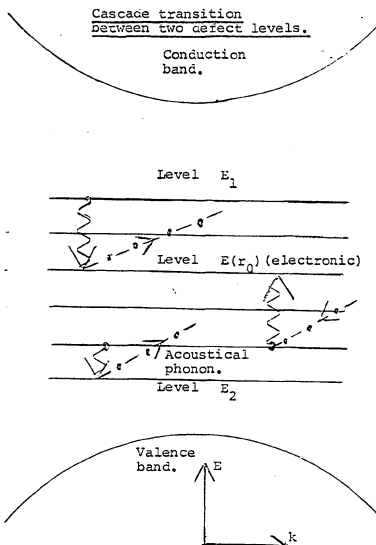

Fig. 1.2.5: Cascade transition between defect levels, from E_1 to E_2. The electron emits an acoustical phonon at each step, making intermediate transitions down a ladder of electronic levels, $E(r_0)$. The transition rate decreases with temperature.

Chapter 2

Steady State Investigation

2.1 INTRODUCTION

There are many variations of steady state spectroscopy useful for studying the dynamics of excited electrons. Steady state photoluminescence(PL) and absorption are commonly used to find the static energy levels, but in this chapter they will also be used to find carrier recombination pathways in SI CdSe(Rosen et. al.,1985). Early studies of semiconductors used nonlinear PL and time resolved spectroscopy(on a microsecond or millisecond time scale) together in order to understand carrier recombination. In a similiar way, the defect levels studied by nonlinear PL in this chapter are also studied by picosecond time resolved spectroscopy in later chapters.

2.2 STANDARD PHOTOLUMINESCENCE: METHODS AND MATERIALS

In figure 2.2.1, the apparatus for measuring PL is shown. An Ar-ion laser(Coherent model 52), tuned to either the 488 nm line or the 514 nm line, was used to excite the sample above the bandgap. The excitation beam was modulated by a chopper(at 100 Hz), focussed on the sample, and then the PL was collected by lenses and directed into a monochromator and measured by a PMT as a function of wavelength. The lock-in system(PAR model HR-8),tuned to the chopper modulation, eliminated most of the background and noise from the measured signal. The monochromator

could be scanned, so that the PL spectra could be recorded by an x-y recorder.

A narrow band dielectric filter(Ditric Optics,Inc.), at the laser wavelength(either 488 nm or 514 nm) filtered the laser radiation. This filter eliminated the spontaneous emission lines from the Ar gas. In front of the monochrometer, a long pass filter was used to block the laser line. When a polarizer was used to select the polarization of the PL, a polarization scrambler was placed between the polarizer and the monochromator to prevent the gratings from changing the polarization values.

The excitation was varied using neutral density(ND) filters(Corning and Hoya), whose transmission at the wavelength of excitation was measured. The intensity of the laser was continuously measured using a power meter(NRC model 815), so that any variation over 5% could be eliminated by tuning the laser. The laser was permitted to warm up at least an hour before each measurement, which slowed down the drift of the laser intensity(≈5%/hour). Every measurement where the excitation intensity I_P was changed was repeated at least four times. The sequence of excitation intensities was repeated forwards and backwards in order to partly compensate for any slight changes in laser intensity. In order to optimize the PL intensity, it was necessary to focus the laser beam to as small a spot size as possible. It was not possible to accurately measure the spot size when this was done, so only relative measurements of excitation intensity are accurate in this study. However, the laser had a maximum power of 200 mW and the spot size was roughly $2 \times 10^{-6} cm^2$, so the maximum

excitation intensity was estimated as $\approx 10^5$ W/cm^2.

In order to check both the linearity of the PMT and the precautions concerning intensity drift, a scatter plate replaced the sample. Then the monochrometer was tuned to the scattered light of the laser. The scattered light was linear with excitation intensity over three orders of magnitude, as expected. This was repeated with scattered light from the sample itself.

The PL measurements were done on five undoped samples of CdSe, supplied by Cleveland Crystals, Inc. . The crystals were grown by the vapor phase technique, in the form of large boules. Each boule contained large, single crystal grains. The starting material contained a large contamination from sulfur(≈2%). Sulfur could not cause any of the defect levels described in this thesis because it is an isoelectric impurity. The samples were cut from different boules, then some of the samples were annealed in Se vapor and then all the samples were chemically polished. Three samples were undoped, SI CdSe crystals annealed in Se vapor(samples will be denoted H_1, H_2 and H_3) and two samples were undoped, unannealed low resistivity crystals(denoted L_1 and L_2). Samples H_2 and L_1 were cut from their boules so that their optical axes(ĉ) were parallel to the surface for polarization studies. The other samples were cut so that their optical axes were perpendicular to the surface. The purpose of measuring the PL of the low resistivity samples, L_1 and L_2, was only to show that the dynamics of electrons were different in SI CdSe and low resistivity CdSe.

A dewar was used for low temperature measurements, where the temperature was measured with a Cu-constantin thermocouple.

Liquid nitrogen was added to cool the samples to 77 K and a cold nitrogen gas flow was used for one polarization measurement at 200 K. An air flow kept the outside surface of the dewar free of condensation.

2.3 NONLINEAR PHOTOLUMINESCENCE RESULTS

The basic idea behind PL is shown in figure 2.3.1. As shown in the schematic, a photon whose energy is larger than the bandgap is absorbed and creates a conduction electron and a free hole. The free carriers(i.e., electrons and holes) relax nonradiatively to the bottom of the conduction band CB and the top of the valence band VB, or into midgap states. These midgap states are usually defect levels, except for a few exciton states. PL occurs when radiative transitions occur between energy levels. The following notation will be used: a transition where a conduction electron recombines with a hole is called a CH transition, a donor electron recombining with a hole transition is called a DH transition, an electron to acceptor transition is called a CA transition, an unknown level to acceptor transition is called an XA transition, etc. Because the above bandgap excited free carriers undergo many transitions before emitting a photon, the polarization and shape of the final PL spectra is decoupled from the energy and polarization of the initially absorbed photons. The experimental PL spectra and polarization were found independent of the wavelength and polarization of the exciting laser light as expected, except for differences in total quantum yield(which depends on the number of

photons absorbed).

The PL spectra is shown, for the SI samples, at 77 K in figure 2.3.2 and at room temperature(300 K) in figure 2.3.3. The PL spectra of each sample showed two major bands at 77 K. The free carrier band, from XH transitions, peaked at 682 nm, and its position relative to the bandgap of CdSe suggested it could be a mixture of CH(conduction electron-to-hole transitions) and DH(shallow donor-to-hole transitions) PL. The other broad band(called here the XA band) peaked at ≈715 nm and is commonly thought to be a mixture of electron-to-acceptor(CA) and shallow donor-to-acceptor(DH) PL(Hatano et. al. ,1979). The XA band indicated a shallow acceptor ≈100 meV above the valence band. As the temperature was raised to room temperature, the XA band disappeared due to ionization of the shallow acceptor state. At room temperature, XH band had shifted to 712 nm, due to the shifting bandgap energy E_g, and broadened as shown in figure 2.3.3. The ratio of XH PL to XA PL was different from sample to sample, probably due to the different acceptor concentrations of these uncontrolled impurities. The spectra of the low resistivity samples were similiar.

The dependence of PL intensity I_L on excitation intensity I_P is shown in figure 2.3.4 for the XH band and 2.3.5 for the XA band. The PL of the XH band obeyed the following power law over two or three orders of magnitude in each case(note that ~ denotes proportionality, while ≈ denotes approximation):

$$I_L \sim I_P^m \qquad (2.3.1)$$

The power law for the XH band were always superlinear(m>1) for all samples. The power law for the XA band was always sublinear(m<1) above a certain threshold intensity and either linear or superlinear below the threshold. This thesis will concentrate on the sublinear region, although this breaking point will be physically explained by the Klasens model. Equation 2.3.1 will be used, within the sublinear region, to find the value of m for the XA band.

The parameter m was constant as a function of wavelength(within each band) to within 5% and did not change with either polarization of the PL or the spatial site on the sample. The value of m did change greatly with temperature, sample and was different for the XH and XA bands. Table 2.3.1 shows m for different conditions, where m was measured at the wavelength of the peak PL intensity for each band. The table shows m only in the sublinear region. The low resistivity samples tended to have a more linear power law(m=1) than the SI samples.

The exponent m was almost constant with wavelength within a band. However, m in the XH band did increase very slightly just below the bandgap energy, in the SI samples. This increase in m was difficult to measure both because the luminescence was weak in this region and because the change in m was itself small. In order to show this increase in m, the following ratio R was determined as a function of wavelength λ:

$$R(\lambda)=I_L(2I_P)/I_L(I_P) \qquad (2.3.2)$$

Here $I_L(I_P)$ is defined as the PL intensity with excitation intensity I_P, and $I_L(2I_P)$ is the PL intensity when the excitation is doubled. The ratio R will obviously increase with m, but does not need as large a dynamic range in I_L as m for accurate measurement.

The ratio R is shown in figure 2.3.6 for sample H_3, the SI sample with the $\hat{c}$ axis parallel to the surface. The following observations were made. First, the increase in R started just below the band edge at both 77 K and room temperature, even though E_g shifted with temperature. The ratio R of the XA band at 77 K was less than 2, indicating the sublinearity described previously. The ratio R was almost constant in the XA band at 77 K all the way to 800 nm. For the total luminescence, there was only one maximum in R, while for $\vec{E}_L // \hat{c}$, there were two maxima. The corresponding increase in m was very small(≈10%). The ratio R will be discussed after the major variations in m, shown in table 2.3.1, are explained.

2.4 NONLINEAR PHOTOLUMINESCENCE THEORY

Three facts show that the nonlinearity in the PL was extrinsic. First, the variation in m from sample to sample shown in table 2.4.1 indicated uncontrollable impurities were involved. For example, at 77 K for the XH band, one SI sample has a value for m of 2, the other samples have values for m of ≈1.5 and the low resistivity samples have a value of 1.2. Second, the sublinearity in the XA band indicated some type of saturation of the shallow acceptor level. Third, no intrinsic mechanism for nonin-

tegral m could be found.

The following models for extrinsic nonlinear behavior were investigated: the model by Klasens(Klasens,1948; Klasens,1958), where only one or two defect energy levels are involved in recombination; the model by Rose(Rose,1963), where a single quasi-continous band of defect levels are involved; and the model by Bube(Cardon and Bube,1964), where more than two defect level bands are involved. The Klasens model, with a slight deviation due to a third defect level band, best explained the previously described experimental results. This model will be described for a simple case, then the characterization code used in this theory will be described, followed by applications of this model to the experimental results. A brief discussion of the other models will then be given.

Klasens solved rate equations under every possible condition where one or two discrete defect levels dominate the recombination process. He only assumed that the concentrations(n_o,p_o) of thermally generated free carriers were negligible compared to concentrations(n,p) of photogenerated free carriers. This is a very reasonable assumption for SI semiconductors(n_o,p_o=$10^7 cm^{-3}$) under steady state photoexcitation(n,p>10^{15} cm^{-3}).

The most common power law in table 2.3.1 is m=1.5, which can be explained by a very simple model. More complex models will be considered further in this section. Consider a semiconductor with a single defect level R and with a total defect concentration N_R, as shown in the schematic of figure 2.4.1. Under above bandgap photoexcitation with intensity I_P, there are n free elec-

trons, p free holes and n_r electrons trapped in R. The optical cross section is u_e, the rate of electron capture by R is controlled by constant c_e and the rate of hole capture is controlled by constant c_h. Every electron in CB or R leaves a free hole in VB. For this case, the following rate equations apply:

$$dn/dt = u_e(N_r-n_r)I_p - c_e(N_r-n_r)n$$
$$dn_r/dt = c_e(N_r-n_r)n - c_h n_r p$$
$$p = n + n_r \qquad (2.4.1)$$

Under steady state conditions, all the rates vanish (i.e., $dn/dt=dn_r/dt=0$). The following specific conditions are now imposed on this semiconductor sample at this excitation: the Fermi level is far below both the energy level R($n_r<N_r$) and the middle of the energy gap($n<<p$). It is seen that $N_r-n_r \approx N_r$ and by the last equation in 2.4.1, $p=n_r$. Solving equations 2.4.1, it is found that:

$$n = (u_e/c_e)I_p$$
$$p = (u_e N_r/c_h)^{0.5} I_p^{0.5} \qquad (2.4.2)$$

Note that equations 2.4.2 will only apply in the range of I_p where $n_r<<N_r$ and where electron capture is the fastest process, i.e., $c_e N_r << c_h p^2$. This range can be extremely wide. The power laws in this range for band to band CH PL intensity, L(CH), CB to R PL intensity, L(CR), and R to VB PL intensity, L(RH), can be obtained from 2.4.3 as shown:

$$L(CH) \sim np \sim I_p^{1.5}$$

$$L(CR) \sim nN_r \sim L(RH) \sim p^2 \sim I_p \qquad (2.4.3)$$

This single center model can explain the 1.5 power law of a CH band, although it does not explain sublinear defect level PL. Sublinear PL implies more than one defect level. It is seen in this example that the superlinearity comes from competing recombination pathways. The nonradiative electron capture does not increase as fast as the radiative electron-hole annihilation, so the quantum efficiency increases with I_p. This "saturation" of defect levels is the basic principal behind nonlinear PL and photoconductivity(PC).

The above model is based on restrictive conditions on the sample. Different samples and excitation intensity ranges can have different power laws. Klasens solved and coded all situations in which at most two localized energy levels exist, where these energy levels can either capture or emit free carriers(Klasens,1958). His model will not be solved for every condition, but his coding system and classification scheme will be described for single defect level and two defect level conditions, in his own notation. Then his coding system will be applied to the experimental results for SI CdSe described in section 2.3.

First, assume a single defect level A below the dark Fermi level(the scheme can be changed for a level above the dark Fermi level). In describing the steady state condition during excitation, the following symbols will be used:

a = total density of recombination centers.

a^0 = density of occupied A levels.

a^+ = density of empty A levels.

n = density of electrons in conduction band CB.

p = density of free holes in valence band VB.

$F = \delta np$ = rate of electrons recombining with free holes.

$I = \beta n a^+$ = rate of empty A levels capturing free hole.

$C = \alpha p a^0$ = rate of occupied A levels capturing free holes.

$L = \gamma a^+$ = rate of thermal release of holes from empty A centers.

U = rate of excitation of free carriers.

An important point is that U is proportional to the laser intensity, F is proportional to the conduction electron to hole(CH) luminescence, I is proportional to the CA defect luminescence and I is proportional to the AH defect luminescence. Using these definitions, Klasens found the following set of simplified equations:

$$\begin{array}{cccc} (1)\ a = a^0 & (1)\ n = a^+ & (1)\ U = I & (1)\ C = L \\ (2)\ a = a^+ & (2)\ n = p & (2)\ U = F & (2)\ C = I \end{array} \qquad (2.4.4)$$

Any particular situation can in general be described by one particular combination of four equations, one out of each column. There are 16 such cases. In referring to these combinations, it is found most practical to introduce a code system. Instead of mentioning each time the set of four equations which describes a situation most faithfully, each combination of equations is designated a code number consisting of 4 digits, each digit indicating which of the 4 equations is appropriate. For instance, a situation indicated by the code number 1112 means that $a = a^0$, $n = a^+$, U = I and

C = I. The solutions for n, p, a^+ and a^0 were solved, by Klasens, and the solutions tabulated. Although these equations will not be solved in this thesis, except for condition 1112, the tables are placed in the Appendix. As shown in table A1, for condition 1112 that $F \sim U^{1.5}$ and $L \sim I \sim U$, as seen by our first example. Thus, the situation described by figure 2.4.1 corresponds to condition 1112.

Each coded condition is appropriate only over a limited range of U: i.e., $U_i<U<U_f$. However, this range of U can be very large,i.e., $U_i<<U_f$. The solutions to the "breaking points" U_i and U_f were solved in terms of the interaction terms (α,β,γ)and total defect concentration(a). The breaking points are shown for the single defect level model in A2. For example, according to A2, condition 1112 is appropriate only for $U_2<U<$the minimum of U_1,U_3 and U_4. Here $U_1 = \beta a^2$, $U_2 = \gamma^2/\beta$, etc. If in this crystal, $U<U_2$, condition 1111 is appropriate(F~U), if $U_3<U_1<U_4<U$, then condition 1122 is appropriate(F~U). So 1112, with $F \sim U^{1.5}$ could be appropriate over a wide range if $U_2<<U_1,U_3,U_4$.

For many situations, a two center model is more valid. Again, each concentration and the luminescence assocoated with it depends on the power of the excitation rate U. In addition to state A assumed in the one center model, assume a second energy level H above the dark Fermi level. In addition to the concentrations and rates defined above, define the following quantities:

h = total density of H levels.

h^- = density of occupied H levels.

h^0 = total density of empty H levels.

$R = \eta p h^-$ = rate of hole capture by electrons in H per unit volume.

$E = \varepsilon n h^0$ = rate of capture of electrons by empty H levels.

$B = \zeta h^-$ = rate of thermal release of electrons from occupied H levels.

For the two defect level model, each experimental condition is coded according to the following set of simplified equations:

(1) $a = a^0$ (2) $a = a^+$

(1) $h = h^0$ (2) $h = h^-$

(1) $a^+ = h^-$ (2) $a^+ = n$ (3) $h^- = p$ (4) $n = p$

(1) $U = I$ (2) $U = R$

(1) $C = L$ (2) $C = I$

(1) $E = B$ (2) $E = R$ (2.4.5)

An important point is that R and E are proportional to luminescence from H(R-PL from hole capture and E-PL from electron capture). All situations that can occur can be approximated by combinations of the six equations above, one out of each row, as indicated by a code number consisting of six digits. Each digit corresponds to one row of the set of equations in 2.4.5 and indicates which equation of the corresponding row is chosen. Each concentration, recombination rate and emission rate depends on a power of U(i.e., if $n \sim U^x$ and $a^+ \sim U^y$, then $I \sim U^{x+y}$), as described for the single level model. The power laws for n, p, I and R are shown in A3.

As an example, consider condition 111212. In this condition, it is seen that $a = a^0$, $h = h^0$, $a^+ = h^-$, $U = R$, $C = L$ and $E = R$. Using the table in A3, it is immediately seen that $I \sim U^{1.5}$, $n \sim U$, and $p \sim h^- \sim U^{0.5}$. Hence the free-carrier both luminescence F

and the acceptor luminescence I are both proportional to $U^{1.5}$, according to 111212.

Condition 111212 is valid only over a limited range in U, from U_i and U_f. The solution to the breaking points for the two center model was solved only for special cases, some given in the tree graph of appendix A4. In the case of 111212, below U_i, F has a power law m=1(code 111211) and above U_f, F could have a power law m=2(code 211212). However, a complete study of the two center model breaking points was not done by Klasens and is not necessary for this thesis.

The Klasens model is based on the most simple physical picture for defect interactions. Its complexity comes from the number of mathematical solutions solved for every possible precondition. The model by Rose and the model by Bube were also considered, but were found not to explain the data.

The single band Rose model assumes a quasi-continuous band of states, as shown in figure 2.4.2,. The density of states, ρ, of this band obeys the following equation:

$$\rho(E)=\rho_o \exp((E_{FD}-E)/(k_B T_R)) \qquad (2.4.6)$$

where E_{FD} is the dark Fermi level and T_R describes the width of the distribution. Equation 2.4.6 only has to be valid over a narrow region of E. An electron Fermi level(not the dark Fermi level) moves through this distribution as the excitation U increases, so that states become saturated and the PL quantum efficiency rises. The PL of the electron to hole(CH) recombination varies with lattice temperature T_L, according to:

$$m = 1 + T_R/(T_R + T_L), \quad T_L < T_R$$
$$m = 1.5 \quad , \quad T_L > T_R \qquad (2.4.7)$$

The Bube model assumes more than two recombination defect centers. At intensities where a third level contributes significantly to the recombination process, the PL rises faster than a square law with excitation and does not obey a power law as described in equation 2.2.1.

2.5 DISCUSSION OF NONLINEAR PL RESULTS

The theory in section 2.4 will now be applied to the results on undoped CdSe in section 2.3. The data can first be used to find out how many recombination centers occur in SI CdSe.

The single band model by Rose does not apply to SI CdSe for three reasons. First, equation 2.4.7 was applied to the values of m shown in table 2.2.1, to find T_R for sample H_1. For sample H_1, T_R had different values at 77 K and 293 K, so the Rose model was not consistent with the experimental results. Second, the ratio R at 77 K was almost constant in the sublinear XA band. If the XA band was PL from a continuous distribution of energy levels containing an electron Fermi level, R would have a sharp discontinuity at the Fermi level. Third, the XA band peaks ≈100 meV below band edge, in agreement with the theoretical value for the ground state of the hydrogenic acceptor, which is a discrete state.

The PL(CH) dependence on excitation, as shown both in figure 2.3.4 and table 2.3.1, was a perfect power law and m was no

greater than 2. Consequently, according to the Bube model, a third recombination center was not a major recombination center. Furthermore, m for the XH bands in the SI samples had values close to 1.5 or 2, as predicted by the Klasens theory. Therefore, two major recombination centers are adequate to explain most of the experimental results in SI CdSe.

As shown in appendix table A1, there are no single center Klasens models where the CH PL has m = 1.5 and the impurity band is sublinear. Furthermore, the XA band shows a breaking point in figure 2.3.5, while the XH band does not in figure 2.3.4, showing one recombination pathway takes over when another pathway has saturated. Consequently, there have to be two recombination centers in SI CdSe, with the shallow acceptor responsible for the sublinear XA band in CdSe as one of the levels. The Klasens model requires that the other level be a deep level. Photoluminescence from the second level could not be found. Other techniques described in this thesis were used to find this deep level.

A third defect level band must serve as a luminescence center(a defect with a high efficiency for radiative transitions) in SI CdSe, though not as a major recombination center. The table in A3 shows that PL(CA) should have power laws of 0.5 or 1. The table 2.3.1 shows an PL(XA) had a value for m of 0.7. This can be explained if the XA PL has a large contribution from shallow donor to acceptor(DA) transitions, where the shallow donor has a slightly higher power law than the free electrons. The contribution of PL(DA) to the XA band is supported by the differences in shape of the XA band from sample to sample, because PL(CA) spectra

would have the same shape from sample to sample. The higher power law for shallow donors is shown by the increase in R below bandgap, if it is assumed that the low energy tail of the XH band comes from PL(DH) and the above bandgap PL comes from PL(CH). Separate shallow donor peaks or discrete DA lines in these samples were not resolved, even at 4 K(Junnakar,private communication). The shallow donors are therefore an inhomogenously broadened conduction band tail, which can not be resolved from the free electrons as a separate peak. It is reasonable to suppose that directly excited shallow donors would decay by thermal emission of electrons, which is a process linear in excitation U. The filled shallow donors are therefore assumed to have a power law dependence closer to linear than the free electrons,i.e., when the conduction electrons have m≈0.5 in table A3, m of the filled shallow donors was assumed to be ≈0.7. This physical assumption explains both the m of the XA band and the slight rise in R below bandgap. This increase in R may have a contribution from bound excitons, but this possibility was not investigated.

With the assumption of two localized recombination centers and another localized luminescence center, all the SI samples at the different temperatures can be characterized according to the Klasens model. The Klasens coded condition for each sample is also included in the table 2.3.1. Consider the case at 77 K for samples H_2 and H_3. There are two conditions in A3 where m ≈ 1.5 for the CH luminescence and m<1 for the XA band: condition 113222 and condition 221221. In condition 113222, the free hole concentration $p\text{-}I_p^{0.5}$ and free electron concentration n is linear, while

in condition 221221, n ~$I_p^{0.5}$ and p is linear. Because the shallow donor concentration d^- is considered more linear in I_p than n, only in 221221 is the DH PL intensity($-d^-p$) more nonlinear than the PL(CH) intensity ($-np$). In condition 221221, the power law below bandgap is predicted to be m=1.7, but in condition 113222, m=1.7. Therefore, condition 221221 is appropriate for H_2 and H_3 at 77 K. At room temperature, all the SI samples have an m(XH)=1.5. Although the PL(XA) is not measurable, model 221221 is assumed valid at room temperature for SI CdSe. For sample H_1 at 77 K, m(XH)=2.0 and m(XA)=0.8=1, which is found in table A3 to correspond to condition 114121. In condition 221221, a = a^+, h = h^-,a^+ = h^-, U = R, C = I and E = B. In condition 113222, a = a^0,h = h^0, h^-=p, U=I, C = I and E = R. Thus sample H_1 seems more compensated than H_2 and H_3(a^+ = h^-), as suggested by the large XA luminescence and large shallow donor absorption that will be described in a later section.

The low resistivity undoped CdSe had power laws for the XH band that were between 1.0 and 1.5, showing that Klasens model does not exactly apply to these samples. This is expected because these samples have a high thermal background of free electrons(≈$10^{16}cm^{-3}$), which violates an important assumption of the model. The XH band is nearly linear in these samples, perhaps due to the higher thermal background of electrons. However, for sample L_1, m(XH)≈1.5 at room temperature, showing that this sample may have been more compensated than the other low resistivity samples. It will be shown in chapter 4 that the shallow donors are important traps in low resistivity CdSe, although a complete

study will not be made of low resistivity CdSe.

2.6 POLARIZED PHOTOLUMINESCENCE STUDIES

The intrinsic symmetry properties of CdSe are well documented(Yoshida et. al.,1981). Cadmium selenide is wurtzite, so it has a maximum allowed symmetry group C_{6V}(see figures 2.6.1 and 2.6.2). The free carrier wave functions of wurtzite solids belong to two important irreducible representations, Γ_7 and Γ_9, of C_{6V}(see fig. 2.6.1). In CdSe, the conduction band belongs to Γ_7. The valence band degeneracy is lifted so there are three valence bands: the heavy hole band (Γ_9), the light hole band(Γ_7) and the split-off band(Γ_7). The minimum energy of holes in the split-off band(0.45 eV) is much larger than the background thermal energy k_BT_L, so there are few holes in this band and the PL from this band is negligible. The heavy hole(Γ_9) and light hole(Γ_7) bands are 27 meV apart, and both contribute to the CH PL previously described. A schematic of these energy levels is given in figure 2.6.1. The selection rules for PL(CH) are as follows: PL from electrons to heavy hole(CH_9) transitions is polarizated perpendicular to the optic axis $\hat{c}(\vec{E}_L \perp \hat{c})$ and PL for electrons to light hole transitions(CH_7) is polarized both parallel and perpendicular to the optical axis($\vec{E}_L \parallel \hat{c}$ and $\vec{E}_L \perp \hat{c}$). The PL(CH_7) is polarized mostly $\vec{E}_L \perp \hat{c}$. The peak of the CH PL spectrum is usually 27 meV higher in photon energy for $\vec{E}_L \parallel \hat{c}$($CH_7$ PL) than for $\vec{E}_L \perp \hat{c}$(CH_9 PL). Studies of the interactions between these valence bands have been done(Yoshida et. al., 1981). However, symmetry can also effect the dynamics

of localized states in wurtzite semiconductors(Birman,1966; Birman,1960).

In order to delineate the symmetry properties of the shallow defect levels and free carrier bands, studies of the polarization of the PL in sample H_2(where $\hat{c}$ was parallel to the surface) were done. The primary interest was in finding out whether the wurtzite structure of CdSe split the shallow acceptor level as it had split the valence band and in finding appropriate selection rules for defect levels. A schematic of possible defect level transitions which involve defects are shown in figure 2.6.2.

At each temperature, the peak wavelength for $\vec{E}_L // \hat{c}$ was ≈10 nm longer than for $\vec{E}_L \perp \hat{c}$, as shown in figure 2.3.2 for 293 K, and at 77 K the XA band did not shift with polarization. At 77 K, a second small peak at 682 nm was observed for $\vec{E}_L // \hat{c}$, probably due to the small(≈5°) collection geometry, the small XH band width and the fact that the selection rules are exact only for normal incidence. Because the bandwidth was larger at higher temperatures, this small peak was unobservable at higher temperatures. At 200 K, the XH band and the XA band was not distinct for $\vec{E}_L \perp \hat{c}$ because the XA PL high energy PL tail overlapped the DH PL band tail, but for $\vec{E}_L // \hat{c}$ the XA peak was very distinct. In both cases it was determined that the peaks of each band were far enough apart that polarization measurements would not be affected.

The tail of the XH band at 293 K was ≈5 nm longer for the $\vec{E}_L // \hat{c}$ case, as shown in figure 2.3.2. The ratio R had one maxima for $\vec{E}_L \perp \hat{c}$, but two maxima for $\vec{E}_L // \hat{c}$. The XH band peaked at different wavelengths $\lambda_\perp$ and $\lambda_{//}$,for $\vec{E}_L \perp \hat{c}$ and $\vec{E}_L // \hat{c}$, while there was

no shift at 77 K for the XA band($\lambda_\perp = \lambda_{//}$). Because there was no shift at 77 K, it was assumed that there was no shift at 200 K even though the peak for $\vec{E}_L \perp \hat{c}$ was indistinct. The polarization for both bands at all temperatures is defined as:

$$p = I_\perp(\lambda_\perp)/I_{//}(\lambda_{//}) \qquad (2.6.1)$$

where $I_\perp(\lambda_\perp)$ is the intensity of the band for $\vec{E}_L \perp \hat{c}$ at $\lambda_\perp$ and $I_{//}(\lambda_{//})$ is the intensity of the band for $\vec{E}_L // \hat{c}$ at $\lambda_{//}$. It was also determined that the polarization of the band, after correction for the shift, did not change with wavelength λ except for the problems described above which could not effect the value of p. The wavelengths, $\lambda_\perp$ and $\lambda_{//}$, of the peak PL for each polarization of each band at each temperature is shown in table 2.6.1. A salient point is that both the CH polarization and the XA polarization were strongly dependent on temperature.

The PL experiments suggest that the XH low energy tail comes from DH transitions, called the Lambe-Klicke model, as shown in figure 2.6.2. The two maxima in R and the longer low energy tail for $\vec{E}_L // \hat{c}$ show that the $PL(DH_9)$ is not completely polarized $E_L \perp \hat{c}$. This means that the shallow donors do not completely belong to representation Γ_7(i.e., that the shallow donor wavefunction has contributions from both the Γ_7 and Γ_9 representations). The shift in the XH peak wavelength corresponds exactly to the valence band splitting of 27 meV. This shows that the $PL(CH_7)$ is completely polarized $\vec{E}_L \perp \hat{c}$ as predicted from the selection rules for a Γ_7 conduction band. Therefore, the shallow donor conduction

band tail does not have the same maximum allowed symmetry as the intrinsic crystal. The simplest assumption one could make about the donor is that it has the same maximum allowed symmetry as the crystal, so some symmetry breaking mechanism must effect the shallow donor. The symmetry of the shallow donor electrons may be broken by their inhomogenous environment,i.e., the core potential of the donor defect, other donors, stacking faults or surface broadening. The shallow donor itself may not be a point defect.

The PL(XA) was strongly polarized, which indicated both splitting in the acceptor and the selection rules for the CH transitions partly apply to the XA PL, but no shift in peak wavelength with polarization was observed at 77 K. A shift of 27 meV in the acceptor peak energy would have been observable, hence the splitting of A is much smaller than 77 K. In order to understand this splitting, it is assumed that the XA PL obeys nearly the same selection rules as for electron to free hole transitions,i.e., Schoen-Klasens model, and that the effect of the donor on the selection rules is small. Schoen and Klasens showed that there are four plausible models for the shallow-acceptor level: two single level models, a spin-split model with each level nearly empty of electrons(i.e., acceptor above Fermi level) and a spin-split model with both levels nearly full of electrons sharing a single trapped hole(i.e., acceptor below Fermi level). By comparing the polarization p in the XA band at 77 K and 200 K, one finds a weak temperature dependence p which eliminates the first three models. The electron empty shallow acceptor is therefore a spin-split defect center nearly full of electrons, with a trapped hole

in thermal equilibrium between the levels, as shown in figure 2.6.2. In order to estimate the small splitting, using p at 77 K and 200 K, the Schoen-Klasens formula was used:

$$p = a \exp(Y/k_B T_L) \qquad (2.6.2)$$

When applied to the intrinsic XH band, Y was found to be ≈15 meV which was comparable with the 27 meV splitting between the heavy and light hole bands. However, Y was ≈1.7 meV for the XA PL. Although only an estimate, the splitting for the A level was much smaller than for the free holes. This may be due to the difference in effective mass between the heavy and light holes. The small splitting is less than the thermal energy $k_B T_L$, and hence the acceptor is only one level as far as the Klasens dynamic model is concerned.

The polarization measurements distinguished the donors from the acceptors. If the XA band was from a donor 100 meV below the conduction band, as measured by DLTS(Ture et. al.,1983), the peak of the XA band would shift with polarization by 25 meV. The peak does not shift, so the XA band comes from an acceptor. Similiarly, if the band tail belonged to the valence band instead of the conduction band, only one maximum in the ratio R would be observed for $\vec{E}_L // \hat{c}$. There are two maxima, so the band tail comes from donors. By the Klasens model, the shallow acceptor and the deep level are on opposite sides of the dark Fermi level. The shallow acceptor is below the Fermi level. Undoped, SI CdSe is always slightly n-type(Heinz and Banks,1956; Hung et. al.,1969). Therefore

the deep level causing the nonlinear luminescence is a deep donor. Although these levels were not seen by DLTS, it is possible that the partially annealed, low resistivity CdSe used in the DLTS studies were different than the completely annealed SI CdSe used in this study.

2.7 STEADY STATE ABSORPTION METHODS

Steady state absorption of SI CdSe, samples H_1 and H_3, was done for three reasons. First, to confirm the assumption that the PL(XA) was due to a discrete defect level ≈100 meV in the bandgap. Second, to find the hypothetical deep donor implied by the measurements. Third, to show that these levels existed in the bulk and were not just surface states.

An apparatus was built for measuring the absorption, as shown in figure 2.7.1. A tungsten lamp was used as a light source because of the required range of wavelength. The light was modulated by a chopper, collimated and refocused on the sample. The transmitted light was collected into a monochromator and measured by a PbS photoresistor(PD). A lock-in amplifier, tuned to the chopper frequency, analyzed the PD signal, which was recorded by an x-y plotter. Each measurement was repeated at least four times and averaged.

Special procedures were necessary because of the large range of wavelengths studied(0.7 μm to 2.0 μm). The sample was removable, so that the spectrum of the source could be measured without passing through the sample. Long pass filters were used

to eliminate high order diffraction from the monochromator. The grating of the monochromator was blazed for 1.0 μm, because gratings blazed at shorter wavelengths did not transmit sufficient signal to measure. The sensitivity of a PMT did not extend as far into the infrared as the PbS photoresistor. Because of the small area of the sample(<1 cm^2) the light had to be focussed through the sample. However, by replacing the sample with a quartz plate of the same thickness, it was found that dispersion effected the transmission for short focal distances(f<20 cm), and so the focussing distances were kept long. In order to collimate the light source, a long focal length lens was used(f>1 m). The transmission had to be corrected for the reflection losses, which depended on the index of refraction, at the two surfaces.

The absorption results could be compared to the PL results at both room temperature and 77 K. A dewar with liquid nitrogen was used to cool the sample. To prevent bubbles and refraction in the liquid from creating errors, the sample was not immersed but was attached to a copper cold finger which was immersed in the liquid nitrogen. The thermocouple showed the temperature of the sample to be 77 K.

If, at wavelength λ, the intensity of the light transmitted through the sample was $I(\lambda)$ and the intensity of the light transmitted through the empty holder was $I_0(\lambda)$, the transmission through the sample is defined as:

$$T(\lambda) = I(\lambda)/I_0(\lambda) \qquad (2.7.1)$$

The physically relevant quantity is the absorption α at wavelength λ. This absorption must be corrected for the index of refraction, $n(\lambda)$, which can be found in the literature(Vitrikhovsky,1967; Bond,1965). If L is the thickness of the sample, the formula for α is:

$$T(\lambda) = T_B(\lambda) \exp(-\alpha L)$$

$$T_B = (1-R)^2$$

$$R = (n-1)^2/(n+1)^2 \qquad (2.7.2)$$

A plot of $T_B(\lambda)$ is shown in figure 2.7.2. The thickness L of sample H_1 was 2.0 mm and of sample H_3 was 1.55 mm. Correction for multiple reflections inside the sample was not made. The resolution of this method was severely limited when $T/T_B=1$(i.e., for $\lambda>1$ μm). However, the resolution was sufficient for proving the existence of a deep level.

2.8 ABSORPTION RESULTS AND DISCUSSION

Absorption thresholds are often more prominent in semiconductors than absorption peaks. Consider the absorption of a photon by a defect electron, which makes a transition to a conduction band, as shown in figure 2.8.1. When the photon energy E is below a threshold E_o, no transition takes place. When $E>E_o$, absorption takes place. As E increases, more transitions to electron states with high kinetic energy are possible so the absorption α increases rapidly. Transitions between defect levels show

peaks, but these are not usually prominent at these high temperatures. Thresholds are also prominent for valence band to defect level transitions. The same transitions often show as peaks in the PL spectra due to nonradiative transitions of carriers to the band edge, as shown in figure 2.3.1. Threshold absorption with a discrete level often shows the following power law above threshold:

$$\alpha(E) = s(E-E_o)^{\nu} \qquad (2.8.1)$$

where s and ν are parameters.

If the absorption is not phonon assisted, ν=1.5, if it is phonon assisted, ν=2(Bourgoin and Lannoo,1983). Although the resolution of this study was not sufficient to determine ν, it was assumed that due to conservation of the photon momentum, a phonon is most likely to be emitted(ν=2) during absorption. It is still not known whether the absorption was phonon assisted. Parameter s is the absorption co-efficient of the defect.

The absorption spectra for the SI samples H_1 and H_3 were measured from 0.6 to 1.8 eV and showed two components, a near-band-edge component and a midgap component. The near-band-edge component was measured as a function of energy below bandgap and is shown in figure 2.8.2, and plotted on a semi-log scale to emphasize sudden changes in slope. The near-edge component showed a very sharp threshold at ≈105 meV below the band edge, where the shallow acceptor to conduction band(AC) absorption was expected. Although the midgap component of absorption was present, the

threshold could easily be found by a broken-line fit. The existence of a threshold shows that the shallow acceptor is a narrow discrete level. The threshold shifted with the temperature because the acceptor moves with the valence band. Above the threshold, the absorption curve for the short component was fitted to the following square law for absorption:

$$\alpha(E) = s(E-E_o)^2+b \qquad (2.8.2)$$

where E_o is the threshold energy, s is the absorption co-efficient of the shallow acceptor A in equation 2.8.2 and b is the deep state absorption of the midgap component. The acceptor ionization energy E_A was calculated from E_o and the energy gap E_g by:

$$E_o = E_g - E_A \qquad (2.8.3)$$

The values of E_A, s and b are shown in table 2.8.1. The parameter s, which would be proportional to the shallow acceptor concentration, shows that H_1 has more shallow acceptors than H_3, in agreement with the small PL(XA) of sample H_3 shown in figure 2.2.1.

The midgap component responsible for b is shown in figure 2.8.3, as a function of photon energy(not corrected for changes in temperature and bandgap). It also shows a threshold, although not as sharp as the near-edge component. Using the broken line approximation to fit the data, as was done for the near-edge component, a threshold of ≈1.3 eV was measured. The deep level

absorption was presumed to come from transitions from the valence band VB to the same deep donor H as was implied by the PL measurements, because if it came from transitions between the conduction band and H, H would be below the dark Fermi level. Thus the energy of the deep donor is ≈1.3 eV above the valence band. Nonlinear absorption work described later suggests this level may extend slightly below 1.2 eV. A salient point is that absorption measurements on thick samples are insensitive to surface states, so both the shallow acceptor and deep level, shown by absorption, are bulk states.

The deep level absorption changed with increasing temperature, as shown both by parameter b in table 2.8.1 and by figure 2.8.2. No theoretical study of the temperature dependence was done. However, if there was no direct transition between deep donor and shallow acceptor, the deep level absorption would not change because the thermal energy is less than the binding energy of the deep donor, while the shallow acceptor ionizes in this range. Therefore, some type of relationship between the two levels may be implied. Perhaps both shallow acceptor and deep donor are charge states of the same atom.

The standard optical techniques described in this chapter showed that a deep donor(≈1.3 eV above the valence band), a shallow acceptor(≈105 meV above the valence band) and a conduction band tail(≈25 meV long) cause recombination of carriers in SI CdSe. An energy level diagram of SI CdSe, showing these defect levels, is shown in figure 2.8.4.

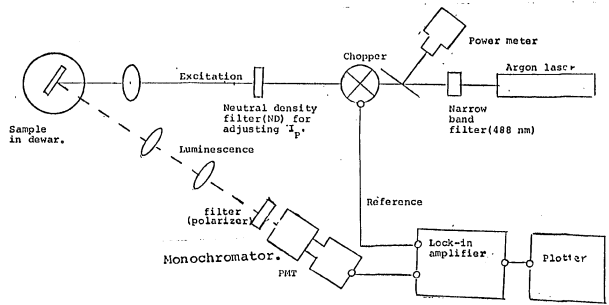

Fig. 2.2.1: Schematic representation of the steady-state photoluminescence set-up.

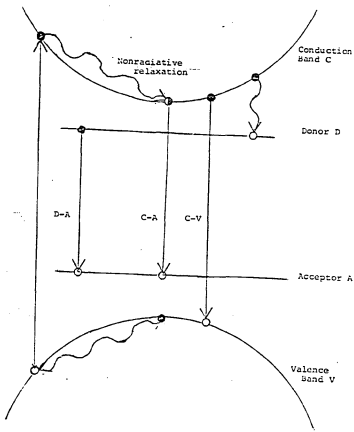

Fig. 2.3.1: Energy level schematic of the photoluminescence process. Vertical straight lines represent radiative transitions and vertical wavy lines represent nonradiative transitions. Radiative transitions are labeled(i.e., C-H, C-A and D-A).

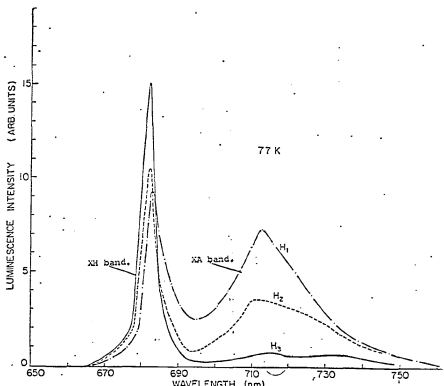

Fig. 2.3.2: Photoluminescence spectra of three samples(H_1, H_2 and H_3) of semi-insulating CdSe at 77 K. Shown are the free hole(XH) and shallow acceptor(XA) bands. Sample H_1(-•-•), sample H_2(---) and sample H_3(——).

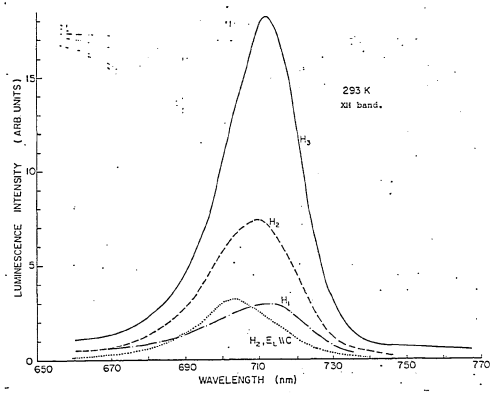

Fig. 2.3.3: Photoluminescence spectra of three samples(H_1, H_2 and H_3) of semi-insulating CdSe at 293 K(room temperature). Only the free hole(XH) band is observable. The component of photoluminescence polarized parallel to the optical axis($\hat{c}$) is shown for sample H_2. Sample H_1(-•-•), sample H_2(---), sample H_2 where $\vec{E} \| \hat{c}$(• • •) and sample H_3 (——).

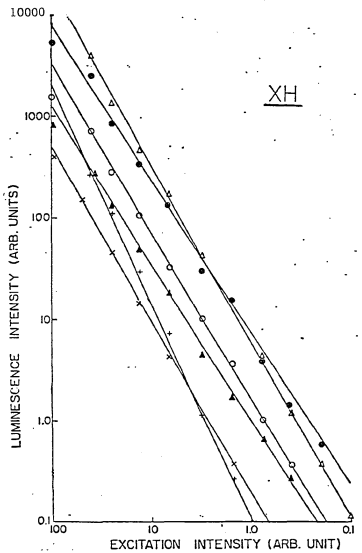

Fig. 2.3.4: Intensity of photoluminescence as a function of excitation intensity, at the peak of the XH band(715 nm at 293 K and 682 nm at 77 K), for different samples of SI CdSe at 77 K and 293 K. Sample H_1 at 77 K(+), H_1 at 293 K(X), H_2 at 77 K(●), H_2 at 293 K (▲), H_3 at 77 K(△) and H_3 at 293 K(○).

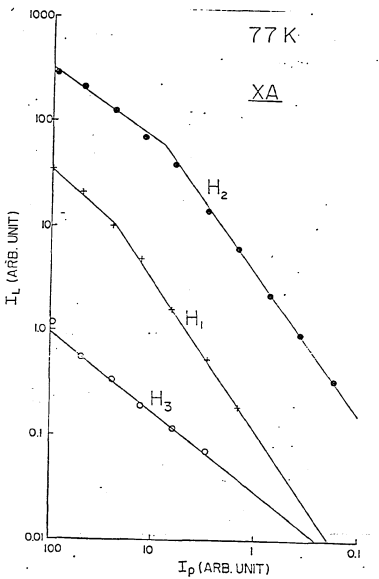

Fig. 2.3.5: Intensity of photoluminescence, I_L, as a function of excitation intensity, I_p, at the peak (~710 nm) of the XA band at 77 K, for three samples of semi-insulating CdSe. Sample H_1(+++), sample H_2 (●●●) and sample H_3(000).

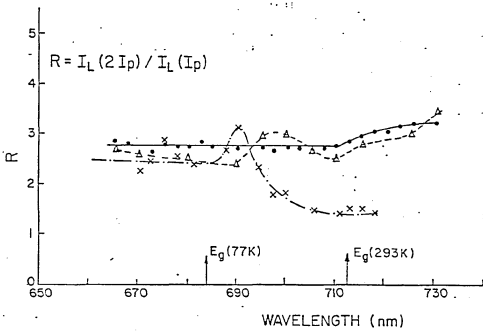

Fig. 2.3.6: The ratio $R=I_L(2I_p)/I_L(I_p)$ as a function of the photoluminescence wavelength for sample H_2. The wavelength corresponding to the energy gap is shown for 77 K and 293 K. The ratio R is shown for three conditions: at 77 K(XXX), at 293 K(●●●) and at 293 K for the component of photoluminescence polarized parallel to the optical axis(ΔΔ).

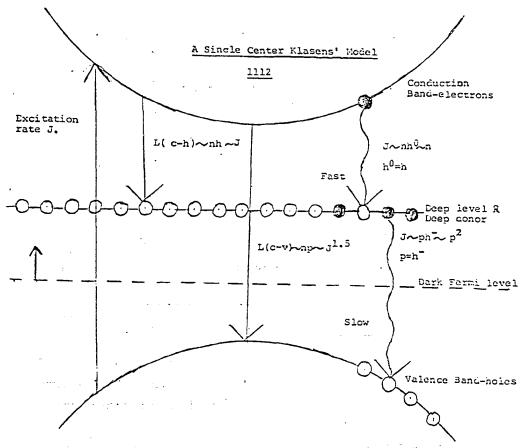

Fig. 2.4.1: Klasens model for a single deep donor level, under condition 1112 as described in the Klasens notation (Klasens, 1958). Under condition 1112, the band-to-band photoluminescence obeys a power law in excitation intensity with m=1.5, while band-to-donor luminescence obeys a linear power law with m=1.0.

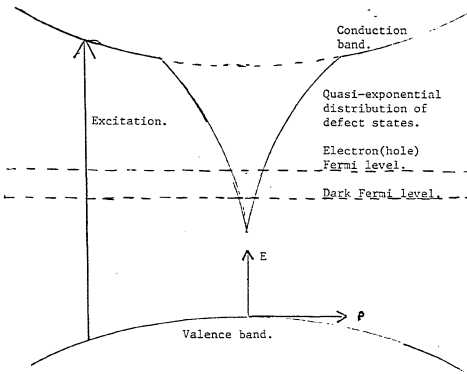

Fig. 2.4.2: Energy level schematic for the quasi-continuous distribution model by Rose. The density of defect states is nearly exponential and an excited state Fermi level(electron or hole) can move through this distribution with changing excitation.

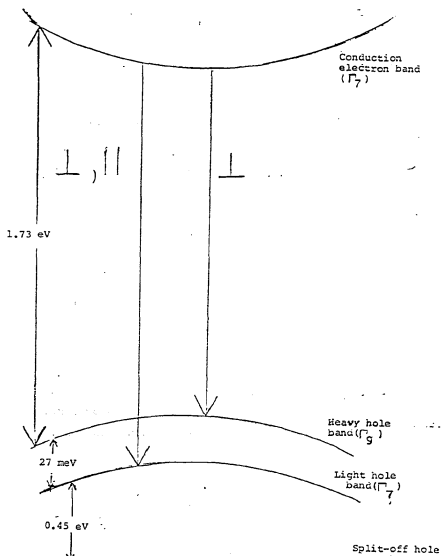

Fig. 2.6.1: Symmetry of energy levels and selection rules of photoluminescence for intrinsic, wurtzite(C_{6v}) CdSe. The polarization of the photoluminescence corresponding to a transition is shown relative to the optical axis.

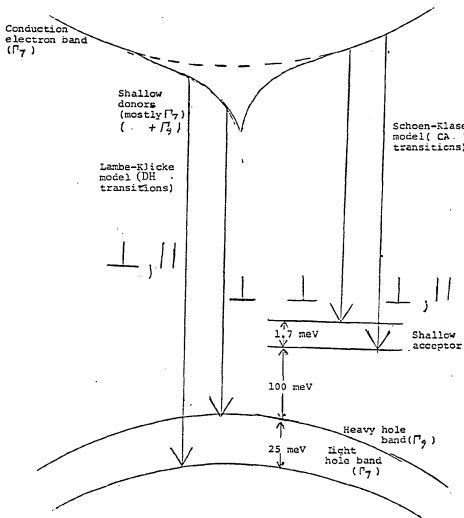

Fig. 2.6.2: Symmetry and selection rules involving shallow defect states in semi-insulating, wurtzite CdSe. Polarization of photoluminescence is shown relative to the optical axis. The selection rules are slightly broken for the shallow donor.

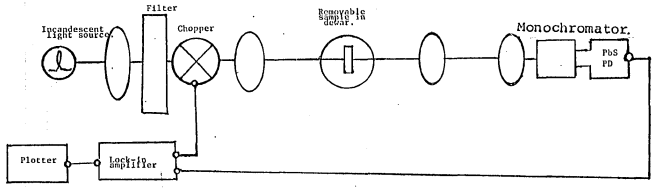

Fig. 2.7.1: Schematic representation of the steady state absorption set-up. A tungsten lamp is the light source. The sample must be removable in order to measure the spectra of the lamp.

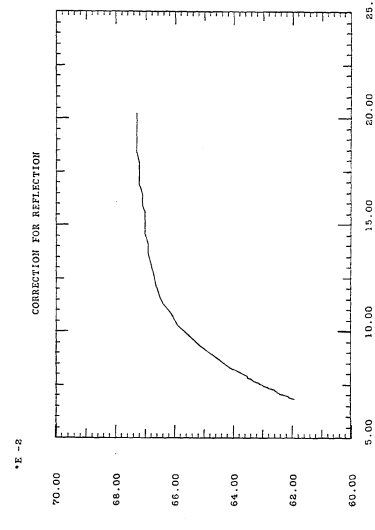

Fig. 2.7.2: The transmission correction factor, TB, due to the surface reflection.

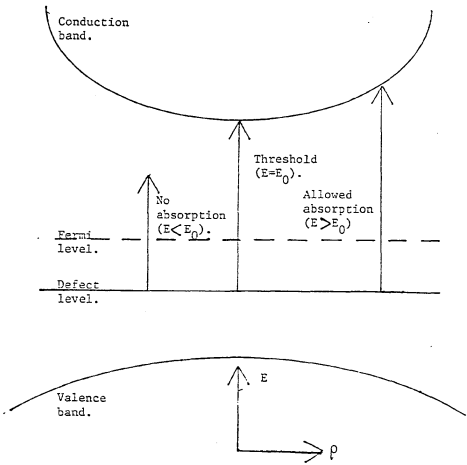

Fig. 2.8.1: Energy level schematic of defect level to conduction band absorption. Below the threshold energy, E_0, optical absorption is not allowed. Above the threshold, absorption is allowed and increases with photon energy, E.

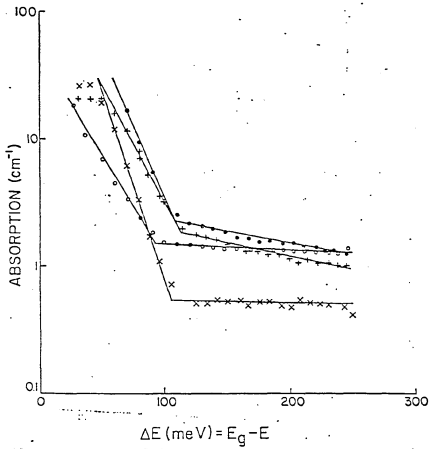

Fig. 2.8.2: Near-band-edge absorption(cm^{-1}) as a function of energy below bandgap, ΔE(meV), for two samples of semi-insulating CdSe at two different temperatures. Sample H_1 at 77 K(●), sample H_1 at 293 K(+), sample H_3 at 77 K(O), and sample H_3 at 293 K(X).

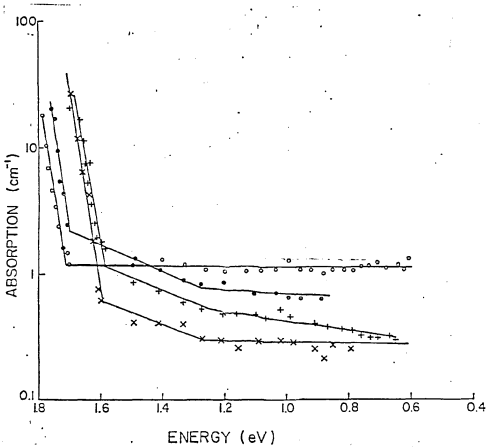

Fig. 2.8.3: Absorption(cm^{-1}) as a function of photon energy for two semi-insulating samples, showing both the midgap absorption threshold ($\sim$1.2 eV) and the near-band-edge absorption threshold(1.6-1.7 eV) at two temperatures. Sample H_1 at 77 K(●), sample H_1 at 293 K(+), sample H_3 at 77 K(O), and sample H_3 at 293 K(X).

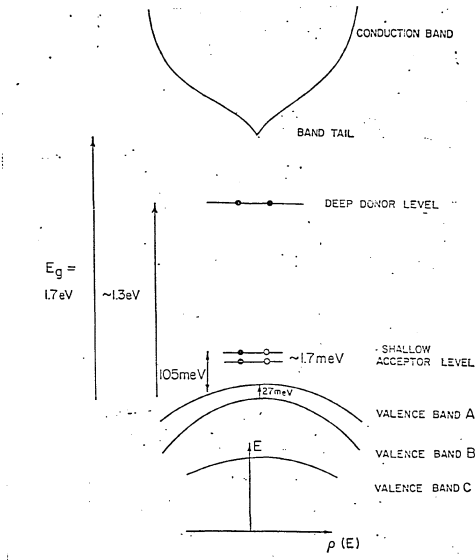

Fig. 2.8.4: Energy level schematic of undoped, semi-insulating CdSe. Shown are the deep donor, shallow acceptor and conduction band tail(shallow donor) states.

SAMPLE	TEMP(K)	m	BAND	* CONDITION
HIGH RESISTIVITY SAMPLES				
H_1	77	2.0	XH	114121
H_1	77	0.8	XA	114121
H_1	293	1.6	XH	221221
H_2	77	1.4	XH	221221
H_2	77	0.8	XA	221221
H_2	293	1.5	XH	221221
H_3	77	1.6	XH	221221
H_3	77	0.7	XA	221221
H_3	293	1.6	XH	221221
LOW RESISTIVITY SAMPLES				
L_1	77	1.2	XH	-
L_1	77	0.9	XA	-
L_1	293	1.6	XH	221221
L_2	77	1.2	XH	-
L_2	77	0.7	XA	-
L_2	293	1.3	XH	-

Table 2.3.1: Power dependence of photoluminescence intensity, L, as a function of excitation intensity, J, according to $L \sim J^m$. The value of m is shown for different samples of CdSe at different temperatures at the peak of the XH and XA bands. Notation for the different conditions is found in Appendix A and in the literature(Klasens, 1958).

Temperature (K)	Band	Wavelength (nm)	Polarization
77	XH	⊥ 682	22
		∥ 673	
77	XA	⊥,∥ 715	6.5
200	XH	⊥ 707	3.4
		∥ 697	
200	XA	⊥,∥ 725	3.0
293	XH	⊥ 715	1.7
		∥ 705	

Table 2.6.1: Polarization of the photoluminescence of semi-insulating CdSe(sample H_2) at different temperatures. The wavelength of the peak photoluminescence for each band is shown for both photoluminescence polarizations, relative to the optical axis. The polarization for each band is defined as the ratio between the peak photoluminescence polarized perpendicular and parallel to the optical axis.

Sample	Temp (K)	Threshold (meV)	$s\ (meV^{-2}cm^{-1})$	$b(cm^{-1})$
H1	77	115	$5.9x10^{-3}$	2.2
H1	293	110	$6.1x10^{-3}$	2.5
H3	77	90	$4.6x10^{-3}$	1.5
H3	293	110	$5.4x10^{-3}$	0.5

Table 2.8.1: Near-band-edge absorption parameters. Parameters E_A, s and b are defined by the following equation for absorption a:

$a = s(E-E_g+E_A)^2+b$

$E_0 = E_g - E_A$

where E_g is the bandgap energy and E_A is the threshold(i.e.,acceptor ionization energy).

Chapter 3

Picosecond Absorption and Polarized Transmission

3.1 INTRODUCTION

Picosecond techniques have been used to study impurities in ionic crystals (von der Linde, 1974; Auston et. al. 1972), but seldom applied to defects in semiconductors. Surface damage on CdSe crystals was shown to shorten the picosecond life-times of free carriers(Huppert et. al., 1982). This chapter describes a picosecond pump-probe study of bulk defects in CdSe. Both induced unpolarized absorption and induced polarized transmission were measured in order to understand the dynamics of photoexcited electrons in SI CdSe.

The direct measurement of picosecond phenomena requires both a picosecond excitation source and techniques capable of using ultrashort pulses. The excitation source used was a passively mode-locked Nd:glass laser. This laser system is a standard tool in picosecond spectroscopy and is extensively described in the literature(Alfano and Shapiro, 1976; Schiller et. al. 1977). This thesis will not concentrate on the laser system itself, but will describe the picosecond measuring techniques that were used to study defects.

3.2 Picosecond Absorption Methods

The picosecond absorption apparatus is shown in figure 3.2.1. A pulse with a wavelength of 1.06 μm (≈7 ps, ≈5 mJ) generated a 0.53 μm second harmonic pulse in a KDP crystal. Both fundamental and harmonic were used to generate a continuum pulse (0.53 μm - 1.06 μm) in a CCl_4 cell. Part of the continuum (the 1.06 μm and 0.53 μm components filtered out)was given a variable time delay and was used as a probe pulse, while part of the 1.06 μm light (≈0.86 mJ) was given a fixed time delay and was used to excite the sample. Both pump and probe pulses were spatially overlapped on the sample within a spot size ≈0.9 mm^2. After each pulse, the energy of the 1.06 μm pump pulse was measured before the sample, while the energy of the probe pulse at a particular wavelength was measured before and after the sample. The pump pulse was measured using a Hadron photodiode (PD), and the probe was measured before and after the sample by separate S-1 photomultipliers(PMTs) in series with separate monochrometers. All three outputs were monitored on a Tektronix 556 Dual Trace oscilloscope. Other investigators, using parametric generation of the probe, measured the absorption induced by a 1.06 μm pump on the probe absorption at 3.4 μm(Ockman and Dorsinville,private communication). The work of these investigators is in progress and some of their results will be compared with the results in this thesis.

The continuum extended from 0.53 μm to 1.06 μm. It was generated by both the 1.06 μm and the 0.53 μm components of the pulse, because if either component was blocked by filters, the

continuum from 640 nm to 810 nm was too weak to use. The continuum is generally believed to be generated by self-phase modulation, but this observation may show that parametric mixing is also important in continuum generation. However, this thesis will concentrate on the study of semiconductors using this continuum pulse as a probe.

In these experiments, the point of zero delay(i.e., the temporal position where the pump and the probe completely overlap) was found by using the optical Kerr effect(Ho and Alfano, 1979). A cell of CS_2, a well known Kerr medium, replaced the sample and was placed between a polarizer and analyzer. This experimental arrangement was used in an experiment described in section 3.6, and is shown in figure 3.6.1. The polarizer and analyzer were crossed, to eliminate the transmission of the probe unless the CS_2 was excited. The 1.06 μm pulse, polarized at 45° to the polarizers, induced a birefringence in the material that permitted part of the probe to pass through the analyzer. If the delay was such that pump and probe pulses did not temporally overlap, transmission was destroyed. The plot of transmission vs delay is shown in figure 3.2.2. This correlation function(between pump and probe) also can be used to estimate the duration of the probe pulse, which was the limiting factor for the temporal resolution. The probe pulse was probably longer than the pump pulse, due to its broad spectrum and dispersion. The pump pulse from this type of laser is $\leq$10 ps long(Alfano and Shapiro, 1976). Thus the width(12 ps) of the transmission curve, shown in figure 3.2.2, agrees with this value. The position and the width of the

transmission were the same for the probe measured at 740 nm and at 790 nm, which means that neither the pulse delay or the pulse width varied in this wavelength range. Dispersion in the experimental apparatus was negligible for this range of wavelengths.

The excitation energy of the pump pulse was varied using Corning(glass) neutral density (ND) filters and Kodak Wratten(gelatin) ND filters. The transmission of the ND filters were measured at 1.06 μm, and agreed with the values claimed by the companies. These ND filters were placed in an expanded part of the 1.06 μm pump in order to prevent filter bleaching. Strongly absorbing filters tend to bleach, so the transmission of each filter chosen was >10%. One glass filter was always used to attenuate the 1.06 μm pulse(all glass filters had equal thickness) to preserve the optical path length. The Wratten filters are very thin, so they cannot change the path length, but they tend to bleach. Wratten filters were only used after glass filters had attenuated the pulse by at least an order of magnitude. The initial pulse energy was kept within ±20% by pulse selection before averaging. Each data point was the average of at least 4 measurements. A long pass filter in the excitation path always eliminated the continuum from the excitation pulse.

Most of the room temperature studies were done on sample H_3, a sample of undoped CdSe which had been previously studied and characterized under steady state, low intensity conditions as described in the previous chapter. The sample had an optical c axis perpendicular to the surface and was 1.55 mm thick. The free carrier and shallow donor band tail luminescence, excited above the

1.73 eV bandgap, had a power law of ≈1.4 in excitation intensity. The absorption at room temperature at wavelength 1.06 μm was ≈0.5 cm^{-1}. This sample, relative to other samples, had a very small shallow acceptor luminescence and shallow acceptor absorption. The sample was kept in the dark during the experiments, in order to prevent photoexcitation by the ambient light.

The room temperature measurements of the pump-probe absorption were repeated on another sample of undoped SI CdSe(sample H_4), because the previous sample started to show slight laser damage marks(i.e., discoloration). The experiments described before remain valid because they were done before the laser damage marks were observable. The room temperature measurements were the same in both samples. The absorption measurements at 790 nm were then done at different temperatures(from 100 K to 293 K), using a cold nitrogen gas flow and heater control system, on sample H_4.

3.3 Picosecond Absorption Results

In time resolved absorption, the induced changes in transmission are measured as a function of time delay of the probe, relative to the pump. Using a beam splitter, the intensity, I_0, of the probe pulse before it enters the sample and after it leaves the sample are measured. Let the intensity of the probe transmitted through the excited sample(pump pulse incident) be I_1 and the intensity of the probe leaving the unexcited sample(pump pulse blocked) be I_2. Then, in anology to equation 2.7.1, the

transmission T of the excited sample, the transmission T_o of the unexcited sample and the fractional change in transmission δT are defined as follows:

$$T_o = I_1/I_o$$
$$T = I_2/I_o$$
$$\delta T = T/T_o \qquad (3.3.2)$$

Every value of T, and every value of T_o, was measured at least 4 times and averaged. The function δT is a function of time delay t. The most physically relevant value is the induced change in absorption $\Delta\alpha$. For the homogenously excited sample of thickness L, the value for $\Delta\alpha$ is given by:

$$\delta T = \exp(-L\Delta\alpha) \qquad (3.3.3)$$

For the inhomogenously excited sample, $\int \Delta\alpha \, dL$ would replace $L\Delta\alpha$.

The induced PL from the pulse could be measured by blocking the probe. This PL peaked at 750 nm, and ranged from 730 nm to ≈760 nm. This anti-Stokes PL will be discussed in a later chapter. This PL created a small background noise problem, but was much weaker than the transmitted probe pulse in the absorption measurements of δT.

The 1.06 μm, 0.8 mJ pulse induced a large increased absorption (OD≈1)for probe wavelengths between 730 nm to 810 nm at t=0 ps. The fractional change in transmission δT of the probe as a function of delay t between pump and probe is shown in figure

3.3.1. The spectrum of δT as a function of wavelength λ from 730 nm to 810 nm in figure 3.3.2, was almost constant, except for a very large luminescence noise background at 750 nm. In this region(730nm-810 nm), the transmission showed a pulse width limited risetime (≈10 ps), a short decay component (≈10 ps) and a very long decay component (≈1 ns). The minimum transmission in all cases was at delay zero, indicating nearly instantaneous excitation. At 3.4 μm, δT was ≈ 0.7 for both long and short components as compared to the small(≈0.1) transmission at 790 nm and 740 nm. This showed that the induced absorption at the shorter wavelengths could not be due to intra-band transitions of induced free carriers, which would increase with wavelength(Pankove,1971). The rapid rise time suggested direct excitation of the defect level. The spectrum fractional change in transmission δT, shown in Fig. 3.3.2, did not significantly vary from 740 nm to 810 nm at 0 ps delay.

The change in probe absorption $\Delta\alpha$ at room temperature was measured as a function of excitation energy J at 0 ps and at 200 ps, and the results are shown in figure 3.3.3. Both could be fitted by a 0.5 power law. This was radically different from the power laws expected from free carrier absorption ,where the carriers are induced by two photon absorption(TPA). An intensity squared dependence for free carrier absorption is expected if the TPA is not saturated and a linear dependence is expected if the TPA is saturated. Saturation of TPA occurs when most of the photons in the pulse are absorbed. The photoexcitation of native defects appears as the most likely explanation for reasons that will

soon be discussed. The increase in absorption, as opposed to bleaching, showed that the excitation and probe absorption started from different ground states.

The time resolved absorption as a function of temperature at 790 nm was measured from 100 K to 293 K. The temperature was varied by a gas flow system. Below 250 K, the short pulse width limited component was not measurable, while the duration of the slow component (τ_K) increased with T_L. The decreasing τ_K(τ_K vs T_L) is shown in figure 3.3.4 and was fitted to the function τ_K-T_L^3, predicted by the cascade theory for two defect levels described in section 1.2.

3.4 Origin of Induced Absorption

In this section, it is shown that the induced absorption arises from defect levels and a physical model is proposed. A later section in this chapter will describe and solve the rate equations for this physical model. The induced absorption from 740 nm - 810 nm, the short wavelength absorption, was shown to originate from excited defect or impurity levels. First, the short wavelength absorption did not significantly change with wavelength. As shown in fig. 3.3.1, the transmission at wavelength 3.4 μm was close to unchanged in value by the 1.06 μm pump, while both the 740 nm and 810 nm wavelength transmission decreased a great deal after excitation. This showed that neither the short nor long components were due to free carrier absorption, because free carrier absorption increases with wavelength(Pankove, 1971). The

absorption was not due to an interband exciton resonance, because the change in absorption at 740 nm, close to the exciton resonance at 715 nm, was nearly the same as the change in absorption at 790 nm(far from the exciton resonance) as shown in figures 3.3.1 and 3.3.2. In addition, the induced absorption of the probe had a very sublinear pump intensity dependence, as shown in figure 3.3.3. Thus, free carriers generated by two photon absorption could not cause the induced probe absorption. Defect levels are the only remaining explanation for the induced absorption. These defect states are probably not surface states, because the probe was transmitted through the bulk of the sample.

The fact that the induced absorption just below bandgap in SI CdSe was not due to free carriers, but was due to native defects, may also be true for other semiconductors. Many previous studies, which assumed that the induced absorption in the crystal studied was due to free carriers or excitons, did not eliminate the possible absorption of excited defect levels(Reintjes and McGroddy, 1973; Becker et. al., 1980; Migus et. al., 1980).

The defect level causing the absorption was a deep level, not shallow levels. The following three observations support this statement. First, the induced absorption extended down to 1.53 eV(as shown in figure 3.3.2), while the bandgap E_g is 1.73 eV, suggesting that these levels were at least 0.2 eV from either the free electron or the free hole band. Second, these levels were directly excited by the 1.17 eV pumping pulse as indicated by the instantaneous risetime of the change in δT as shown in figure 3.3.1. Third, the two step excitation of the conduction band,

which will be discussed in the next chapter, indicated a level was located between 0.56 eV and 1.17 eV above the valence band. Neither the shallow donor or shallow acceptor have energies in this range. The deep donor will be assumed to cause the induced absorption.

The model proposed will use the same energy levels as described in chapter 2 and shown in figure 2.8.4: the conduction band CB, the valence band VB, a deep donor recombination center R responsible for most of the picosecond induced absorption and a shallow acceptor A. The steady state work suggested that a conduction band tail made of shallow donors may also play a minor role. The effect of the band tail is considered negligible in this chapter, but will be studied further in the next chapter. The concentration of total deep donors(including empty donors), deep donors filled with electrons, shallow donors electrons, free conduction electrons and free holes will be denoted N_R, n_R, n_t, n and p, respectfully. A shallow acceptor site can either be empty or contain an electron. The empty acceptor sites will be called trapped holes. The concentration of trapped holes will be denoted p_a and the concentration of acceptors N_a. Let J be the energy of the 1.06 μm excitation pulse.

The initial absorption step, of a 1.06 μm photon, is assumed to be the transition of a valence band electron into R, leaving a free hole. A salient point is that the absorption increased after excitation, i.e., there was no bleaching from 730 nm to 810 nm. Therefore, absorption of a probe photon in this range is assumed to cause a transition from the now filled R state to the

conduction band as shown in figure 3.4.1. The threshold of absorption for the deep donor R was shown in chapter 2 to be ≈1.3 eV, however, there was a small residual absorption (≈0.5 cm^{-1}) below this threshold. This residual absorption is seen in figure 2.8.3, especially for sample H1. Sample H1 had a large defect concentration as shown by the large absorption above threshold. In other semiconductors, absorption below threshold of a deep level is caused by transitions between defect levels and by inhomogenous broadening of the deep level(Sturge,1962). This statement is supported by the fact that the shallow donor T was inhomogenously broadened into a band tail by ≈25 meV, as shown in chapter 2 and chapter 4. Therefore, the assumption will be made that the deep donor R was slightly inhomogenously broadened so that a 1.17 eV photon (the pump) can excite an electron into the deep donor R from either the valence band or the shallow acceptor A. In this model, the change in absorption $\Delta\alpha$ is proportional to n_r, so according to figure 3.4.1:

$$\Delta\alpha(J) \sim p = n_r \sim J^{0.5} \qquad (3.4.1)$$

Both $L\Delta\alpha$ for a homogenously excited sample and $\int \Delta\alpha dL$ for a inhomogenously excited sample would obey the same square root dependence.

The square root intensity dependence in equation 3.3.1 usually indicates, in kinetic models, the rapid recombination of a minority carrier through an unsaturated defect level(Klasens,1946; Wise and Klasens,1948; Klasens et. al.,1948). Because of this

square root dependence, it is necessary to assume that p>>n and that $N_r, N_a >> p, p_a$.

Once the initial defect level excitation mechanism was established, recombination pathways were considered in order to explain slow and fast components of absorption and luminescence. The square root intensity dependence of absorption can only be explained if a non-radiative recombination of free carriers and defect levels takes place during the pulse, in the bulk of the sample. However, an explanation was then needed to explain why this fast recombination stops, so that there are electrons in R left for the slow(1 ns) component of absorption. Band-to-band Auger processes are negligible for large bandgap semiconductors such as CdSe(Landsberg,1959) and the quantum efficiency of the PL was small, so neither Auger or radiative transitions can explain the components of the picosecond absorption. The slow component can be explained by donor-acceptor transitions between R and A and the short component by VB to R transitions(i.e., free hole capture). Transitions between R and A would be much slower than free hole capture, because of the distance between R and A sites. In this model, the fast component decay stops when all the free holes in VB are used up, while the trapped holes in A remain to cause the slow component. The energy level schematic for this model is shown in figure 3.4.1. Two step absorption will be considered negligible in this chapter, but will be measured will be discussed in chapter 4. The transition process for the slow component is shown to be cascade by the temperature dependence, shown in figure 3.3.4. The ladder of electronic states required by the

cascade theory may be part of the inhomogenously broadened deep donor. This ladder will not be studied in this thesis.

3.5 Phenomenological Model

A quantitative theory explaining the different temporal components of absorption will now be discussed. Two photon absorption and electron-hole recombination will not be included in this model. Experiments and models including these weaker effects will be described in the next chapter. Let the pulse width be t_p, the pulse energy be J, and q be the pulse intensity. The rates $\mu_h N_r q$, $\mu_a N_r N_a q$, $c_h n_r p$ and $c_a n_r p_a$ represent the rates of optical excitation of R from VB, optical excitation of R from A, the capture of free holes by R and the nonradiative transfer of electrons from R back to A, respectfully. Screening could change the parameters in this model, but it could not change the rate equations themselves. The rate equations for the processes described before are:

$$\begin{aligned} dn_r/dt &= \mu_h N_r q + \mu_a N_r N_a q - c_h n_r p - c_a n_r p_a \\ dp/dt &= \mu_h n_r q - c_h n_r p \\ n_r &= p + p_a \end{aligned} \tag{3.5.1}$$

The fractional change in transmission, δT, was derivable from n_r using the optical absorption cross section μ_o at the probe wavelength for electrons in R according to:

$$\delta T = \exp(-\mu_b n_r L) \tag{3.5.2}$$

These equations were solved both analytically, using approximations, and numerically by computer. Analytically, the fast component was derived by setting the derivatives in 3.5.1 equal to zero. Then, it was found that:

$$n_r(t) = (N_r(\mu_a c_a^{-1} + \mu_h c_h^{-1}))^{0.5} q^{0.5} j^{0.5} \tag{3.5.3}$$

in agreement with both the short component decay and the power dependence of the absorption. For the second time component, the assumptions were made that q=0 and p=0. The solution to equation 3.5.1 is then:

$$dn_r/dt = -c_a n_r^2 \tag{3.5.4}$$

in agreement with the slow component in figure 3.3.1.

The temperature study approximated the slow component decay as an exponential decay(i.e., $\tau_K^{-1} = c_a n_r$ for t=0). The increase of τ_K with temperature was explained by a cascade process between R and A. The cascade theory assumes that the electron is transferred through a series of intermediate electronic levels by emitting acoustical phonons. Although a series of levels extending from R to A is not probable, a rate limiting step may occur between levels in the inhomogenously broadened R band. The following temperature dependence between defect levels would be expected(Lax, 1959):

$$c_a = \kappa T_L^{-3} - \tau_K^{-1} \qquad (3.5.5)$$

This fits the temperature dependence of τ_K well, as shown by the experimental data shown in figure 3.3.4.

Equation 3.5.1 was solved numerically by computer, assuming a Guassian pulse pulse(i.e., $q(t)=q_o \exp(-t^2/t_p^2)$). The computer programs used are shown in appendix B. The pulse width of the laser system was estimated as 7 ps and the pulse intensity q_o(for an 870 μJ pulse) as 7×10^{29}photons $s^{-1}cm^{-2}$. From the absorption measured at 1.06 μm in chapter 2, $\mu_h N_r \approx 0.5\ cm^{-1}$. The ratio of fast component absorption to slow component absorption then determined that $\mu_a N_r N_a \approx .005\ cm^{-1}$. The transmission at the beginning(at t=30 ps) of the slow component determined $\mu_o \approx 2\times10^{-17}cm^2$. As shown the computer fit in figure 3.5.1, the curve fit the data at room temperature very well for $c_h \approx 5\times10^{-5}\ cm^3/s$ and $c_a \approx 3.7\times10^{-8}\ cm^3/s$. Note that the small values of $\mu_a N_r N_a$ and c_a explain why transitions between R and A were insignificant in the steady state work. The computer curve fit the data at 100 K very well, as shown in figure 3.5.1, with $c_a=10^{-6}cm^3/s$ and with the other parameters unchanged. This supports the model of a cascade transfer from R to A. Using the values of c_a in equation 3.5.5, $\kappa=10^{-12}cm^3s^{-1}K^{-3}$.

The computer solution clearly shows that the free hole capture causes the fast component of absorption and the R-A transfer causes the slow component of absorption. A comparison of $n_r(t)$ and p(t), shown in figure 3.5.2, shows that the slow component starts when $p\approx0$. The R-A transfer parameter, c_a, only

effects the duration of the slow component, as shown in figure 3.5.3. This figure shows that the time dependence of the transmission curves are almost the same, before 50 ps for three different values of c_a, but have different slow components. Similiarly, the free hole capture parameter, c_h, only effects the fast component as shown in figure 3.5.4 for three different values of c_h. The dependence of n_r on q was shown by computer to obey a square root law, which confirms the analytical solution.

The cross section σ_h for hole capture was estimated from c_h and the thermal velocity v_t according to(Bourgoin and Lannoo, 1983; Neumark and Kosa, 1983):

$$c_h = v_t \sigma_h \qquad (3.5.6)$$

The thermal velocity v_t at t=0 was $\approx 3\times10^7$cm/s(equivalent to a carrier temperature $T_C \approx 1800$ K, as described in the next chapter), and the computer simulation fit data for $c_h = 5\times10^{-5}$ cm^3/s, so $\sigma_h = 1.5\times10^{-12} cm^2$. This is higher than other hole capture cross sections, such as $Si:In^-$, where $\sigma_h \approx 1.5\times10^{-13} cm^2$ at 100 K (Lax, 1959) and to $GaP:O^{2-}$, where $\sigma_h = 10^{-14} cm^2$ at 300 K(Henry and Lang, 1977). The largest source of error for the calculated hole capture cross sections in CdSe is probably the measured values of v_t, which assumed a thermal distribution for free carriers. However, the actual cross sections must be very large. The capture cross section of free holes in this experiment may be enhanced in the case of CdSe by the high phonon densities generated by the hot carriers. The rapid capture of free holes described in this model

would explain why steady state, below bandgap PC in CdSe has never been measured as p-type or negative(Bube,1963; Fowler,1961). Photogenerated holes would be captured before they could effect the conductivity. Auger processes which include a defect level could be fast, but would not give the correct power laws for the induced absorption and the anti-Stokes luminescence(described next chapter).

An analogous model, using a deep donor trap and a deep acceptor recombination level fits this data. Such levels were found by DLTS measurements, where the donor has an ionization energy of 0.12 eV and the acceptor has an ionization energy of 0.6 eV(Ture et. al.,1983). In this model, the fast decay component(<20 ps) comes from the capture of conduction electrons instead of free holes. However, photo-Hall measurements on undoped, SI CdSe show that only conduction electrons are generated(i.e., n-type PC) by below bandgap excitation(Bube,1961; Fowler,1961). If the deep level captured conduction electrons as rapidly as the fast component indicates, then n-type PC could not occur. Also, the cross section for electron capture($\approx 10^{-13} cm^2$) by the deep acceptor is too small to explain the fast component decay. Therefore, the two levels involved in the picosecond decay are probably not the same as the levels found by DLTS, and are probably the shallow acceptor and deep donor described in chapter 2. The partially annealed CdSe samples used in the DLTS measurements may have different levels than the SI samples used in this thesis. Another possibility is that DLTS and optical spectroscopy are sensitive to different defect levels.

3.6 Picosecond Polarization Experiments

The dynamics studied previously only describe transitions between defect states at different energies. The dynamics of electron transfer between degenerate levels of a defect can produce resonant enhancement of opto-electronic properties. The picosecond polarization experiments on sample H_3 at room temperature were done to investigate this possibility. Sample H_3 had $\hat{c}$ axes perpendicular to the surface, which eliminated background birefringence effects.

Picosecond induced polarization experiments were performed on this sample under the same conditions as the absorption experiments using the same pump and probe apparatus which measured absorption. The polarization of the continuum was initially parallel to the polarization of the 1.06 μm pump. The sample was placed between a polarizer and an analyzer, which were usually crossed and at 90° to each other, as shown in figure 3.6.1. The polarizer changed the polarization of the probe entering the sample and the analyzer measured the change of polarization of the transmitted probe. When the polarizer and analyzer were crossed, no transmission through the unexcited sample was measured. Each polarizer could be separately rotated, to separate different induced polarization effects. When the polarizer and analyzer were crossed, with the pump polarization either parallel to the polarizer or circularly polarized, the probe transmission through the excited sample was blocked. This eliminated contributions from induced optical activity and induced circular dichroism. When the

polarizers were crossed and the pump polarization made an angle 45° with each polarizer, the 1.06 μm pump induced a polarization in the sample resulting in probe transmission at 790 nm and at 0 ps delay. The large background induced absorption raised the possibility of linear dichroism(Waldeck and Cross,1981). With the polarizer at 45° to the pump polarization, the analyzer was rotated and the polarized transmission T' was measured as a function of angle, θ, between the pump electric field and the analyzer. The induced polarization transmission T' as a function of θ is shown for both the excited and the unexcited sample in figure 3.6.2 at 790 nm and 0 ps delay. The unexcited sample showed a minimum transmission when the two polarizers were at 90°, indicating that the natural birefringence of the material was insignificant. The shift of the minimum T' from the position of crossed perpendicular polarizers by 15° indicated a positive induced linear dichroism (induced absorption greatest in the direction of the pump electric field). The increase in width of the angular profile of transmission indicated an induced birefringence stronger than the dichroism. The physical meaning of induced birefringence and induced dichroism will be discussed in a later section.

The polarized transmission was measured as a function of time and wavelength. The induced polarized transmission, both unnormalized(T') and normalized(T'/T) for the changes in unpolarized transmission(T) is shown as a function of delay t in fig. 3.6.3. The induced polarization did not have a slow component, and after a correction for sample absorption was maximum at zero delay and was pulse width limited (≈8 ps). The polarization

measured as a function of λ and shown in figure 3.3.2, was almost constant from 740 nm to 810 nm at zero delay, except for a very large PL noise background at 750 nm. Because the PL was unpolarized, there was a significant noise signal from the PL even at 790 nm, which was measured by blocking the probe. There was also leakage through the crossed polarizers, which was measured by blocking the excitation pulse. Neither effect was large enough to invalidate the results of this section.

3.7 Discussion of Picosecond Polarization

The physical interpretation of the polarized induced transmission will now be discussed. Induced birefringence is the difference between the index of refraction for light polarized parallel to the pump electric field, $n_{//}$, and perpendicular to the pump electric field, $n_{\perp}$. Birefringence does not change the amplitudes, $A_{//}$ and $A_{\perp}$, of the two electric field components, but it does add a phase delay δ between them. Induced dichroism refers to the difference between the absorption induced perpendicular and parallel to the electric field of the pump, $\alpha_{\perp}$ and $\alpha_{//}$. Dichroism alone does not change the phase delay δ, but it does change the ratio $A_{\perp}/A_{//}$. Consequently, induced birefringence changes a linearly polarized probe to an elliptically polarized probe, while induced dichroism rotates the plane of polarization of the probe. This was used earlier in this paper to distinguish between them. Both require degenerate energy levels(i.e., different wave functions with the same energy). However, induced birefringence

requires only virtual transitions to these levels while induced dichroism requires real transitions to these degenerate levels, so dichroism implies midgap(i.e.,defect) degenerate energy levels.

Consider the crystal between polarizer and analyzer, with an induced polarization as in the experiment previously described. The crystal has a thickness L(0.155 cm), a strong birefringence , a weak dichroism , and is probed by a pulse that is linearly polarized at $45°(A_{//}=A_{\perp})$ to the induced optical axis. The analyzer is at an angle θ to the optical axis. The emerging probe is elliptically polarized, where the angle of the semi-minor axis of the ellipse is at an angle Φ to the optical axis, where Φ is the minimum transmission angle for the analyzer. The polarization ellipse for this situation is shown in figure 3.7.1. The appropriate equations for the emerging pulse are then(Waldeck and Cross,1981; Ayral, et. al. 1984; Yariv and Yeh, 1984):

$$T'/T=\sin^2\delta \text{ where } \delta=2\pi L\Delta n/\lambda \text{ and } \theta=\Phi$$

$$\tan 2\Phi = 2A_{\perp} A_{//} \cos\delta/(A_{\perp}{}^2-A_{//}{}^2)$$

$$A_{\perp}/A_{//} = \exp(-(\alpha_{\perp}-\alpha_{//})L) \qquad (3.7.1)$$

Note the case of zero dichroism($A_{\perp}=A_{//}$). Using the third equation, either $\Phi=45°$(semi-minor axis unchanged)or $\delta=90°$(circular polarization). So any shift in angle Φ after excitation implies induced dichroism, as stated previously. Estimates of these induced effects were made using the following measurements in (3.7.1). At $\theta=\Phi=30°$, $T'/T=0.5$ so $\delta\approx45°$, so using 3.7.1 it is found that $\delta\approx45°$ and $\alpha_{//}-\alpha_{\perp}\approx5\ cm^{-1}$.

Material parameters were be estimated. Induced dichroism is known to be a four-wave mixing effect(i.e., proportional to E_{pump}^2). The optically induced birefringence must also be a four-wave mixing effect, because any effect linear in E_{pump} would average to zero because of the oscillating field E_{pump},i.e., the following equations can be used:

$$\Delta n = K\lambda E_{pump}^2$$
$$\alpha_{\parallel} - \alpha_{\perp} = Sq \qquad (3.7.2)$$

Using q as 10^6 MW/cm^2, the dichroism constant S was found to be 5×10^{-4} cm^{-1}MW^{-1} and the Kerr constant K was 1.5×10^{-19}m/V^2. The dichroism, as stated before, was certainly related to midgap defect states, but origin of the Kerr effect is still not certain. The induced polarization extended through the same region as the induced absorption previously described, suggesting that the same defect levels may have enhanced the induced polarization. The fast picosecond decay of the transmission T', shown in fig. 3.6.1, eliminated the possibility of induced photorefraction. The absence of circular dichroism and optical activity showed that off-diagonal nonlinear effects(i.e., four-wave mixing without an induced $\hat{c}$ axis) were negligable in this experiment(Yariv and Yeh,1984). As with many absolute measurements, a large uncertainty comes from the intensity measurements.

The mechanism for induced dichroism(and probably the birefringence) involved the dynamics of the defects. The response time of the birefringence (≈8 ps) was pulse width limited, just

like the fast absorption component. Some theories predict that deep levels in semiconductors could enhance the Kerr effect because of saturation of degenerate states(Chang,1981; Perlin, 1981). The fast response time of the induced dichroism and birefringence indicate an ultrafast redistribution between degenerate states of the R level. This possibility is shown in the schematic of figure 3.7.2. In this figure, degenerate levels in R preferentially absorb different polarizations of the probe, causing induced dichroism. A similiar model using virtual transitions instead of absorption can explain the Kerr effect. The existence of picosecond four-wave mixing from defects suggests the use of semiconductor impurities by resonant enhancement of phase conjugation.

Models using the deep donor and shallow acceptor explain all the results of the pump-probe experiments described in this chapter. These models describe the recombination of free holes, but do not include electrons in the conduction band. In the next chapter, both the affect of defects on the conduction band and multi-photon absorption will be investigated.

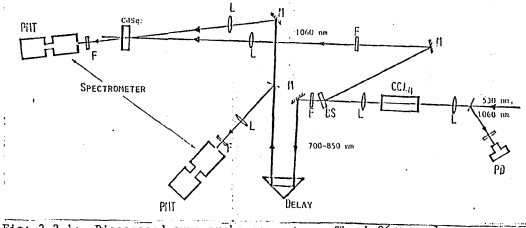

Fig: 3.2.1: Picosecond pump-probe apparatus. The 1.06μm pulse was generated by a Nd: glass laser, and the 0.53μm second harmonic was generated in a KDP cell. All other wavelengths were generated in the CCl_4 cell shown.

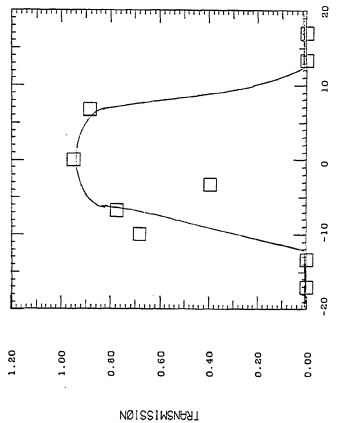

Fig. 3.2.2: Pulse width measurement. Transmission vs delay time for CS2 Kerr cell.

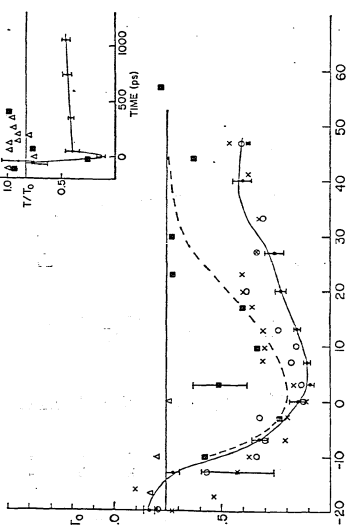

Fig. 3.3.1: Fractional change in transmission, T/T_0, as a function of delay time for different conditions of excitation pulse energy, probe wavelength and temperature: 2.5 mJ, 3.444m and 293 K(ΔΔ); 1 mJ, 790 nm and 293 K(●●); 1 mJ, 740 nm and 293 K(XX); 0.1 mJ, 790 nm and 293 K(OO); 1 mJ, 790 nm and 77 K(■■).

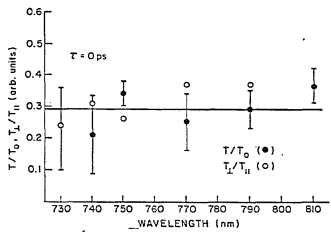

Fig. 3.3.2: Transmission spectra, at 0 ps delay, for both the unpolarized absorption and the polarized transmission experiments. Both polarized and unpolarized induced change in transmission were constant from 740 nm to 810 nm.

Unpolarized absorption experiment, showing the ratio T/T_0 (●●) between the transmission of the excited sample and the transmission of the unexcited sample.

Polarized transmission experiment, showing the ratio T'/T_0 (○○) between the transmission through crossed polarizers and the transmission through uncrossed polarizers for the excited sample.

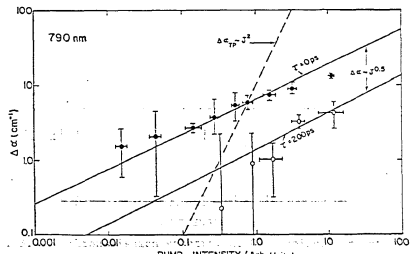

Fig. 3.3.3: Induced change in absorption, $\Delta\alpha$, at 790 nm as a function of pump pulse energy, J, at 0 ps delay(●●) and at 200 ps delay(○○). Also shown is the predicted change in absorption, $\Delta\alpha_{TP}$, for the absorption of free carriers induced by unsaturated two photon absorption.

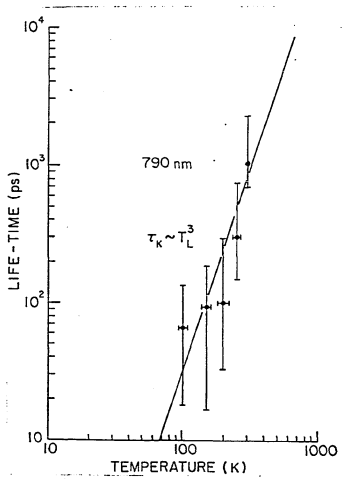

Fig. 3.3.4: Life-time, τ_K, of absorption(slow component) as a function of lattice temperature, T_L. An exponential decay is used as an approximation of the slow component. The data is compared to a cubic temperature dependence, predicted by the cascade theory.

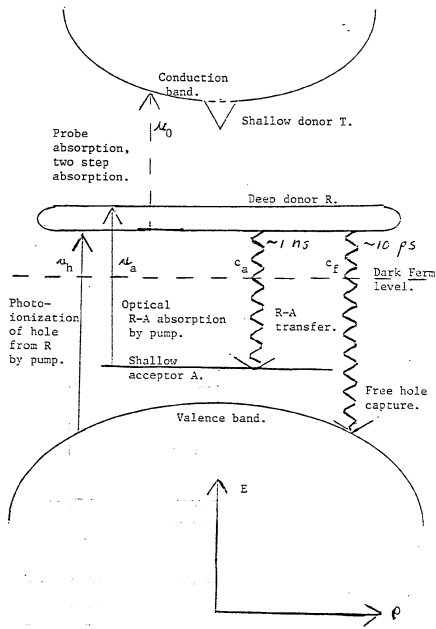

Fig. 3.4-1: Energy level schematic explaining the pump-probe absorption measurements.

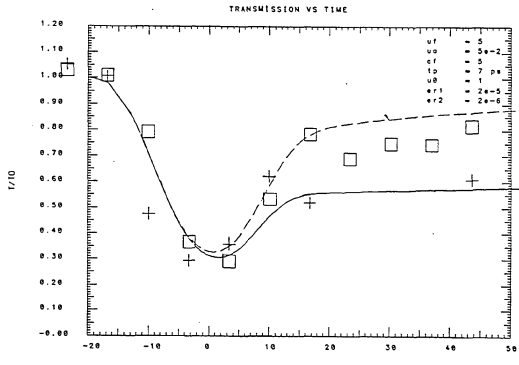

Fig. 3.5.1a: Computer curves for two c_a values compared to the experimental values at two temperatures within the first 50 ps. Except for c_a, the other parameters are fixed at the values stated in the text. $c_a=3.7\times10^{-8}cm^3/s$(——), 293 K(+), $c_a=10^{-6}cm^3/s$ (---), 100 K(□).

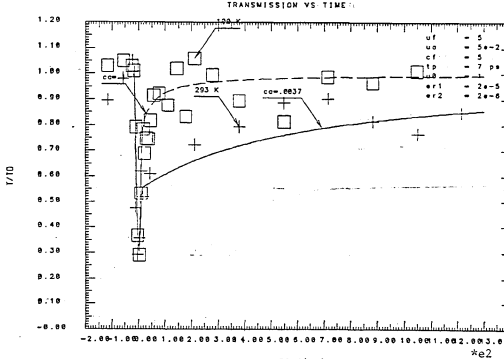

Fig. 3.5.1b: Computer curves for two c_a values compared to the experimental values at two temperatures, over a range of 1.3 ns. Except for c_a, the other parameters are fixed at the values stated in the text. c_a=3.7x10^{-8}cm^3/s(——), 293 K(+), c_a=10^{-6}cm^3/s (---), 100 K(□).

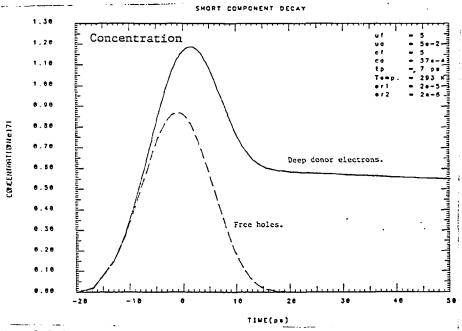

Fig. 3.5.2: Computer generated decay curve of deep donor electrons(——) compared to the decay curve of the free holes(---). The excitation pulse is assumed to be 7 ps wide. The free hole decay is nearly pulse width limited.

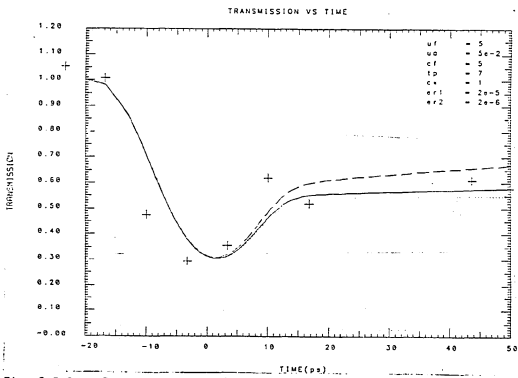

Fig. 3.5.3a: Computer generated curves for different values of c_a, over a range of 50 ps, compared to the room temperature data(+). c_a=1.0x10^{-8}cm^3/s(•), c_a=3.7x10^{-8}cm^3/s(——), c_a=1.5x10^{-7}cm^3/s(---).

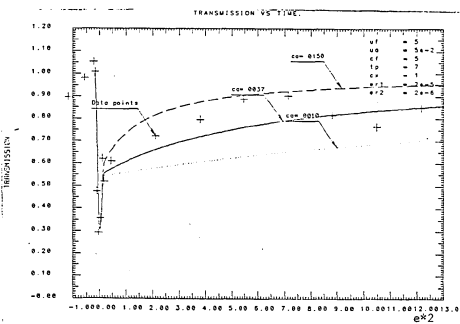

Fig. 3.5.3b: Computer generated curves for different values of c_a, over a range of 1.3 ns, compared to the room temperature data(+). c_a=1.0x10^{-8} cm^3/s(•), c_a=3.7x10^{-8} cm^3/s(——), c_a=1.5x10^{-7} cm^3/s(---).

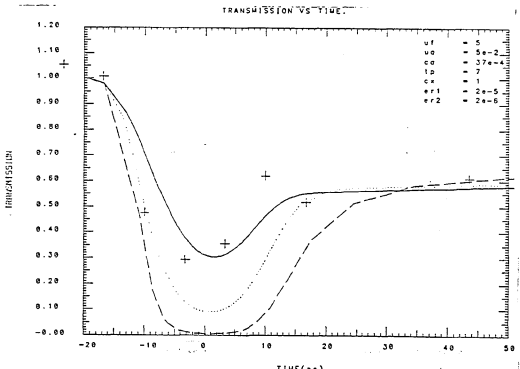

Fig. 3.5.4a: Computer generated curves for different values of c_h, compared to the room temperature data(+), in the range of 50 ps. c_h=2x10^{-6}cm^2/s(---), c_h=10^{-5}cm^2/s(•), c_h=5x10^{-5}cm^2/s(——).

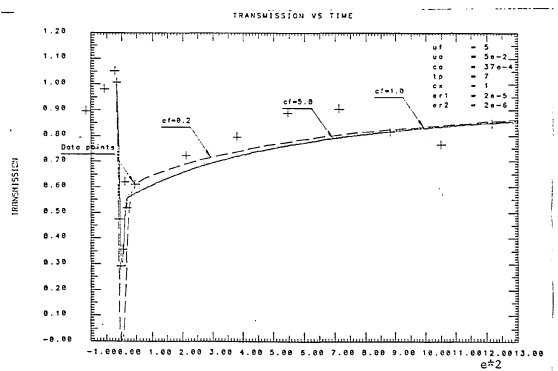

Fig. 3.5.4b: Computer generated curves for different values of c_h, compared to the room temperature data(+), in the range of of 1-3 ns. c_e=2x10^{-6} cm^2/s(---), c_h=10^{-5}cm^2/s(• • •), c_h=5x10^{-5} cm^2/s(——).

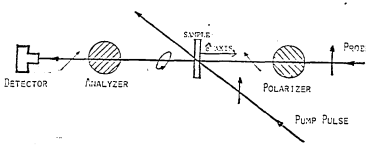

Fig. 3.6.1: Apparatus for measuring picosecond induced polarized transmission. Sample was placed between a polarizer and analyzer. The induced transmission T' was measured when the polarizer and analyzer were crossed. The CdSe sample was replaced with a CS_2 cell to find the position where the pump and probe paths had 0 delay.

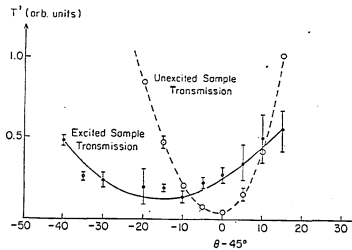

Fig. 3.6.2: Induced transmission, T', as a function of angle, θ, between the 1060 nm excitation pulse polarization. Polarizer was at 315^0 to the pump pulse polarization, so at $\theta=45^0$, the polarizer and analyzer were crossed. Excited sample(●●), unexcited sample(○○).

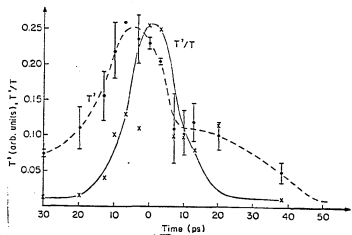

Fig. 3.6.3: Induced polarized transmission through crossed polarizers, T'(--●--), and the ratio T'/T(—x—), where T is the unpolarized transmission. The ratio T'/T shows the induced polarization corrected for the large induced absorption.

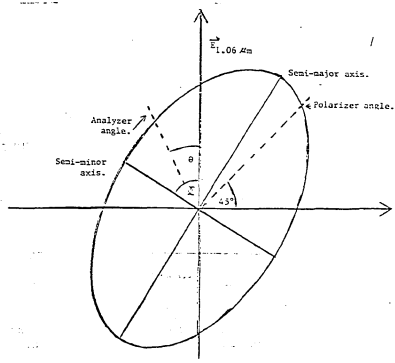

Fig. 3.7.1: Polarization ellipse, showing angle Φ of the semi-minor axis and angle θ of the analyzer. Polarizer is fixed at 315^0. Note that when $\Phi=\theta$, T' is at a minimum. When no dichroism exists, $\Phi=45^0$.

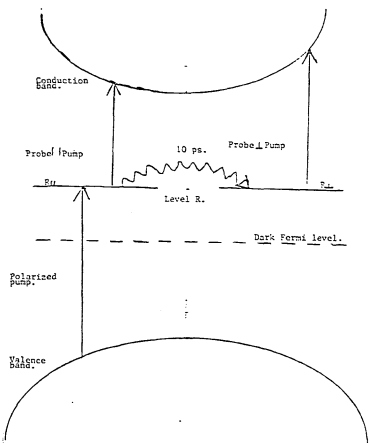

Figure 3.7.2: Energy level diagram for explaining picosecond induced dichroism. Energy level R preferentially absorbs different polarizations of light into different degenerate levels. Once excited, the electrons in R redistribute among the degenerate levels within picoseconds.

Chapter 4

Nonlinear Transmission and Anti-Stokes Luminescence

4.1 INTRODUCTION

The experiments discussed in the previous chapters were done with the explicit purpose of studying the dynamics of defect level electrons in SI CdSe. They showed that these samples of undoped CdSe were highly compensated, and could not be approximated by an intrinsic crystal. Uncontrolled defects could distort measurements of intrinsic properties, such as nonlinear absorption or exciton life-time. This chapter describes experiments on multi-photon absorption and the anti-Stokes PL to show how uncontrollable defects could effect commonly measured properties. Furthermore, the optical recombination rates of the conduction band electrons, that were measured by these experiments, explains the low concentration of thermal carriers in SI CdSe.

Some of these experiments separated contributions from two photon absorption and two step absorption, as shown in figure 4.1.1. In both processes, two photons are absorbed by an electron which moves from the valence band to the conduction band. Two photon absorption is an intrinsic process where the photons are simultaneously absorbed, using a virtual intermediate level(Bechtel and Smith,1976; Reintjes and McGroddy,1973). Because this level is a virtual step, conservation of energy does not determine its energy and so it is usually an intrinsic energy level. In two step absorption, the electron is first excited from the valence band to

a real level, and then from the real level to the conduction band. Because each step must conserve energy, below gap two step absorption implies a defect state. The existence of two step absorption would indicate that defects and impurities could enhance nonlinear absorption.

4.2 LONG LIVED TRAPS

During the absorption measurements described in section 3.2, when the probe was blocked, a small anti-Stokes (AS) PL was detected from the back surface of the photoexcited sample. The spectra of the PL at room temperature, shown in figure 4.2.1 for sample H_3, peaked at 750 nm and extended from 740 nm to 770 nm. The steady state absorption of CdSe,as shown in figure 2.8.2, indicates that the short wavelength cut-off was probably due to self-absorption. The self-absorption indicates that the number of photoexcited conduction electrons was small near the back surface of the sample. A small number of conduction electrons in the bulk of the sample was previously assumed in the model for absorption decay. Steady state PL measurements of the ratio R, described in chapter 2, had previously identified the PL in this spectral region as coming from a transition between the conduction band tail and the valence band.

In order to study how Se-vapor annealing changes the dynamics of electrons in undoped CdSe, the PL from the SI samples of CdSe were compared with the PL from one sample of low resistivity CdSe. In all the SI samples, the decay time of the PL was less

than the time resolution of the dual trace oscilloscope used(i.e., <40 ns). However, sample L_2, which was a low resistivity(LR) sample that had not been annealed in Se vapor, had a PL with a decay time of 200 ns which could be measured by oscilloscope. The oscilloscope traces for the PL at 745 nm are compared in figure 4.2.2 for high and low resistivity CdSe. A slow component of decay at 710 nm will be discussed in section 4.5 for SI CdSe. However, this component is nearly the same(≈2 ns) for both SI CdSe and LR CdSe(Foresti,private communication; Junnakar,private communication). This shows that the streak camera does not have the sensitivity or temporal range to detect the very slow component of LR CdSe at 750 nm.

The oscilloscope measurements showed that a major difference between the dynamics of electrons in SI CdSe and undoped, low resistivity(LR) CdSe is that the shallow donors in the LR CdSe have an extremely slow temporal component of decay. This shows that annealing CdSe with Se-vapor reduces the concentration of long lived, shallow donor traps. The presence of these long lived traps in LR CdSe explains why the Klasens theory did not usually apply to these samples, as was shown in the steady state PL work of chapter 2. The long lived traps probably contribute to the thermal concentration of conduction electrons in LR CdSe. The short decay time of PL in SI CdSe showed that long lived traps do not play a major role in the dynamics of electrons in SI CdSe, and therefore will not be carefully discussed in this thesis. The response time of a semiconductor, which is caused by long lived traps, often limits the speed of an electronic device(Rose,1963).

Therefore, the short response time of SI CdSe may indicate that SI CdSe would be useful in ultrafast electronics. The existence of a slow component of decay caused by long lived traps has been studied by time resolved PC in inhomogenous n-type CdSe(Starostin and Serdyuk,1975; Starostin and Vakarov, 1980).

4.3 NONLINEAR ANTI-STOKES LUMINESCENCE

The AS PL photons had a much larger energy(=1.66 eV) than the excitation photons(1.17 eV), so that this PL was excited by a nonlinear absorption process. Therefore, the AS PL could be used to distinguish between intrinsic and extrinsic nonlinear absorption. The following two assumptions were made. First, the response time of the PL in SI CdSe was much shorter than the time resolution of the oscilloscope, so that the magnitude of the signal in SI CdSe was proportional to the time integrated (TI) PL. Second, that the emitting states of the AS PL at room temperature came from the conduction band tail. This assumption was based on the PL work in chapter 2 and the response time measurements in the last section.

The dependence of the TI PL(745 nm) on pump energy was measured, for sample H_3 at room temperature, to distinguish between the two step and two photon excitation. In chapter 2, the power law of the conduction band tail (T) for all SI samples was shown to be slightly higher than for the band to band PL. The power law of the band to band PL in sample H_3 was 1.4, for the Stokes PL, excited in a single step above the bandgap. The AS PL of the conduction band tail obeyed a power law of =2, as seen in the lumi-

nescence vs J curve at 750 nm in figure 4.3.1, which eliminated direct two photon direct absorption because a two photon process would cause a power law of =3(twice the steady state value of 1.4) in the long pulse limit and a power law of 4(the square of the two photon square law) in the short pulse limit(Braunstein and Ockman, 1964; Halsted et. al., 1977).

The mechanisms of two stage excitation can now be deduced, as described in the model shown in figure 3.4.1. This model was used to explain the absorption measurements in chapter 3, where instead of the absorption of a second pump photon, a probe photon was absorbed. This model predicts that the density of shallow donor electrons, n_t, would be proportional to both the energy of the excitation pulse, J, and to the density, n_r, of electrons in the deep donor(i.e., $n_t - n_r J$). This was shown experimentally as follows. The luminescence L_t from levels T obeyed the following power law, as shown in figure 4.3.1:

$$L_t - n_t p - J^2 \qquad (4.3.1)$$

Using equation 3.4.1, where $p - J^{0.5}$, and equation 4.3.1, where $n_t p - J^2$, the conduction band tail density n_t is found proportional to $J^{1.5}$. However, according to equations 3.4.1 and 4.3.1, $J^{1.5} - n_r J$. This shows that $n_t - n_r J$, as predicted by the model. Thus, the simplest model for two stage excitation, that a valence band electron moves into the conduction band via the recombination center, is confirmed experimentally. An alternate method of finding two step excitation was used, in order to confirm the results

found by nonlinear AS PL.

4.4 NONLINEAR TRANSMISSION STUDIES

In order to study multi-photon absorption of valence electrons into the conduction band, the transmission of the 1.06 μm excitation pulse and the band-to-band luminescence induced by the excitation pulse were measured.

The transmission of the pump pulse was measured after blocking the probe pulse. A scatter plate was placed after the sample, as shown in figure 4.4.1, so that the transmitted 1.06 μm pulse could be redirected and measured by the same system measuring the probe. The monochrometer was adjusted to measure the 1.06 μm scattered light. The oscilloscope revealed a large contribution from stray pulses that leaked through the pulse selector, so a saturable absorber cell was used to absorb these weak intensity pulses. Nonlinear effects of the plate were not involved because the sample absorbed most of the pulse and because the scatter plate was placed so that pulse was not focussed on scatter plate. The linearity of the detector was measured by removing the sample. At high intensities, a photodiode was more linear than the PMT. Both detectors were used within their range of linearity, so that a large dynamic range of intensities could be measured. The absolute intensity of the pulse was calibrated using a Hadron energy meter. The absolute transmission and the absolute excitation intensity had larger uncertainties than the relative measurements, using these procedures. It should be noted

that the entire spatial profile of the pulse is sampled this way, so that nonlinear defocussing could not change the results(Guha et. al., 1985).

The 1.06 μm pump transmission, T, was measured as a function of pump energy J. The data was fitted by least squares to the following formula for intrinsic two photon absorption(Reintjes and McGroddy, 1973; Reintjes et. al., 1975; Stewart and Basa, 1980):

$$T^{-1} = a + bJ \qquad (4.4.1)$$

where T, J, a and b are in arbitrary units.

The ratio 1/T vs J is compared in figure 4.4.2 with a theoretical fit from equation 4.4.1. The least squares fit showed that the best parameters were a=2.32, and b=0.93, with a coefficient of correlation r^2=0.71. The poor graphical fit and the small r^2 indicated that the model for equation 1 was not valid. The ratio 1/T seemed to fit a simple power law of 0.5 better (r^2=0.91) as displayed in figure 4.4.1. One concludes that some type of two step excitation, as opposed to two photon excitation, was significant under these conditions. Equations for two step excitation depend on the nature of the intermediate level.

The same model that explains the AS PL explains the transmission data. If Beer's law is assumed, where $\Delta\alpha$ is the induced absorption at 1.06 μm by electrons in level R and L the sample thickness, then:

$$T^{-1}=\exp(L\Delta\alpha)\approx 1+L\Delta\alpha\approx 1+k_c J^{0.5} \qquad (4.4.2)$$

which can explain the sublinear fit of T^{-1} in figure 4.4.1 and confirms the model used in section 4.3 and chapter 3.

Both the nonlinear PL and nonlinear transmission measurements imply a large contribution from two step absorption. A large two step absorption implies that the first step in absorption is large and that intrinsic two photon absorption is small. The small steady state absorption($\approx$0.5 cm^{-1}) and the high two photon co-efficient (3.5 $MW^{-1}cm^{-1}$) of CdSe do not support this result. However, the optical absorption of deep state R may be enhanced by the surface potential, high carrier temperatures, optical phonon concentrations or plasma densities generated during the pulse. Other investigators have found two step absorption in II-VI semiconductors under conditions similiar to the experiments discussed(Stewart and Basa,1980; Zyul'kov et. al.,1983; Halsted et. al. 1977).

4.5 STREAK CAMERA PL METHODS

Picosecond band-to-band PL, at room temperature, was studied by streak camera for three reasons. First, the effect of the deep donor on the picosecond PL was demonstrated. Many previous studies of picosecond PL in CdSe have been done, usually at very low temperatures, and the results applied to the free exciton theory(Boicko et. al. ,1978; J. Shah, 1974; H. Yoshida et. al. 1981). The defect levels described in this thesis could have introduced errors in these exciton studies. Second, the capture of conduction electrons was measured in order to compare with the capture of

holes described in chapter 3. This was important because SI CdSe has neither thermal electrons nor thermal holes, so defects must capture both carriers. Third, the PL was used to measure the temporal behavior of the carrier temperature to compare with the lattice temperature used in chapter 3. The streak camera technique has been used and described by many investigators, so this thesis will concentrate on the results of these measurements(N. H. Schiller and R. R. Alfano, 1982; R. R. Alfano, 1984).

The free carrier luminescence of sample H_3, excited by a 1.06 μm pump pulse and measured from the front of the sample, was time resolved at 710 nm and 660 nm at room temperature with a Hamamatsu streak camera. Narrow band filters(±5 nm) were used to select the wavelength of luminescence. The maximum intensity of excitation, as measured by photodiodes, was about one order of magnitude larger than in the absorption experiments. Neutral density filters were used to vary the excitation intensity. A salient point is that the absorption of CdSe at 710 nm and 660 nm is greater than 10^4 cm^{-1}, so that the luminescence can be detected only within 1 μm below the surface, although the 1.06 μm pulse penetrates much deeper. The excitation near the surface would be more highly excited than the bulk. The maximum energy of the pulse in the streak camera measurements was measured by Hadron energy meter to be ≈8 mJ.

The sample was much more highly excited in the streak camera experiment than in the absorption experiments for two reasons. First, the excitation pulse energy used in the streak camera experiment(≈8 mJ) was an order of magnitude larger than in the

absorption experiments(≈0.8 mJ). Second, the PL was measured by the streak camera from the highly excited front surface of the sample. The penetration depth of the luminescence at 710 nm and 660 nm is about 0.3 μm, proving that the streak camera examined PL entirely from the front surface. The two photon absorption co-efficient is ≈0.025 cm/MW in CdSe(Bechtel and Smith, 1976; Stewart and Basa, 1980). This co-efficient may involve both two photon absorption and two step absorption. Using the power of the pulse, $\approx 10^5$ MW/cm^2, the penetration depth is calculated to be ≈4 μm, so the front surface was more highly excited than the bulk. A salient point is that the concentration of conduction electrons was much greater on the front surface of the sample than near the back surface. The AS PL measured from the back surface was self absorbed for λ<730 nm, as shown in figure 4.2.1. However, the PL measured by the streak camera from the front surface was very strong at 710 nm, indicating radiative, electron-hole recombination.

4.6 STREAK CAMERA RESULTS AND DISCUSSION

The PL at 710 nm, near the bottom of the free carrier band, showed a fast component (≈100 ps), whose duration was weakly dependent on pump intensity, and a slow component (2.0 ns) independent of pump intensity as shown in figure 4.6.1. The fast component of PL was far slower than the fast component of the absorption. The luminescence L as a function of time t, was fitted to the following empirical formula:

$$L(t)=A_F\exp(-\frac{t}{\tau_F})+A_L\exp(-\frac{t}{\tau_L}) \qquad (4.6.1)$$

where the decay constants of the fast and slow components, τ_F and τ_L, and their amplitudes, A_F and A_L, are shown in 4.6.1 table for both band edge luminescence at 710 nm and hot carrier luminescence at 660 nm for sample H3. The strong above bandgap luminescence at 710 nm showed that many electrons and holes were generated on the surface. In this experiment, zero time is considered the peak of the luminescence.

The fast component of the PL was used to estimate the thermal velocity, v_t, used in chapter 3 to estimate the hole capture cross section. The temporal profile of the free carrier luminescence at 710±10 nm and 660±10 nm(the difference between photon energies ΔE is 0.132 eV) is shown in figure 4.6.2. The calculated plasma temperature T_C, is also shown in figure 4.6.2, where T_C was calculated by the Maxwellian formula:

$$\frac{L(660\ nm)}{L(710\ nm)}=\exp(-\frac{\Delta E}{k_B T_C}) \qquad (4.6.2)$$

The free carrier temperature, T_C, started at 1800 K and decreased to room temperature with a decay time of ≈55 ps, as shown in figure 4.6.1. High carrier temperatures in semiconductors are usually generated by free carrier band-to-band Auger transitions or by excitation high in the free carrier bands. The carrier temperature decays by phonon emission. Sources of error for T_C include Auger processes, screening and a non-Maxwellian distribution of free carriers. Because band-to-band Auger processes are negligible in large bandgap semiconductors, T_C is independent of excitation intensity and so would be nearly the same in both

absorption and streak camera measurements. The high carrier temperature only lasted 55 ps, which was much shorter than the slow component of absorption τ_K, so the temperature study in chapter 3 was not be affected by the hot carriers. Screening could have slowed down the hot carrier cooling in the streak camera experiments, but hot carriers could not influence the slow components of absorption and PL. The largest source of error is probably the Maxwellian distribution assumed in equation 4.6.2, which may partly explain the high value of σ_h found in chapter 3.

Band-to-band PL could decay four ways: direct electron-hole recombination, diffusion into the bulk, recombination through an intermediate exciton state or recombination through defect states. The intensity dependence of the fast component, shown in table 4.6.1, showed that the fast component decayed either by direct recombination or diffusion. The slow component was not intensity dependent, which showed that it was due either to free exciton recombination or recombination through a defect level. At room temperature, the thermal energy (26 meV) was much larger than the free exciton binding energy(15 meV), so that excitons would dissociate much faster than they could recombine. Consequently, the slow component of band edge PL decay must come from defect level recombination. These crystals were chemically polished, which reduces the surface recombination(Huppert et. al,1982). The experiments described in chapters 2 and 3 suggested that the PL recombination was dominated by bulk defect levels. It will now be shown that the same defect levels described previously could explain the PL decay at the band edge(710 nm). The

effect of the surface on the defect levels will not be studied in this thesis.

A model is used to explain the streak camera PL measurements which is different from the model used in chapter 3. The model for the streak camera experiments has to include a high concentration of conduction electrons. The model in chapter 3 assumed the concentration of conduction electrons is smaller than the concentration of the deep donor, which may not be true at very high excitation used for the streak camera. At high intensity excitation, direct electron-hole recombination must be included(i.e., term wnp). Furthermore, at very high excitation, $p>>N_r$, p_a so $n=p$. Because $c_h>>c_a$, the shallow acceptor is considered negligible. The conduction band tail is considered negligible because of the results in chapter 2. Conduction electrons are assumed to be captured by empty deep donor levels(i.e., term kn), but the free hole capture measured in chapter 3 is so fast that the deep donor is expected to remain nearly empty. Then the high intensity rate equations after the pulse($q=0$), using only the deep level R, are:

$$n=p$$

$$dn/dt=-kn-wn^2$$

$$k=c_eN_r=c_e v_t N_r \qquad (4.6.3)$$

The PL intensity L(t) follows the standard bi-molecular recombination equations, with a slow component and a fast component. The PL near the band edge(≈710 nm) is proportional to n^2, so that for t very large where $wn<<k^{-1}$, the following exponential

decay is a solution to 4.6.3:

$$L(t) = A_L \exp(-t/\tau_L)$$
$$2k=\tau_L^{-1} \qquad (4.6.4)$$

which describes the slow component in empirical equation 4.6.1. This slow component was nearly the same in the LR samples, showing that the deep levels in SI and LR CdSe are similiar.

The value of the slow component decay time(τ_L=2 ns), used in 4.6.4, gives k^{-1}=4.0 ns. The fast component is expected to change with intensity(τ_F^{-1}=wn), as shown in table 4.6.1. This thesis will focus on the slow component because it was caused by defects. To estimate c_e, the concentration of the deep donor N_r is assumed $\approx 10^{18}$ cm^{-3}(a typical solubility for an impurity in a crystal), so that $c_e \approx 2.5\times10^{-10} cm^3 s^{-1}$. Note that $c_e << c_h$, so the R could never be saturated with electrons because every captured electron in R immediately recombines with a free hole. The cross section for electron capture, using the room temperature thermal velocity v_t=2.5x10^7cm/s, is calculated as $\sigma_e \approx 10^{-17}$ cm^2. The largest source of error in calculating c_e is probably caused by the estimated concentration N_r. The energy level schematic in figure 4.6.3 shows how direct band-to-band recombination and recombination through the deep donor explains the two temporal components in the streak camera measurements. The recombination of conduction electrons by the deep donor and the absence of long lived traps(described in section 4.2) together explain the high resistivity of SI CdSe.

This chapter has shown how conduction electrons in SI CdSe are both optically excited and recombine through the deep donor. The experiments in chapters 3 and 4 have directly measured the rates that the deep donor R captures free holes, acceptor bound holes and free electrons.

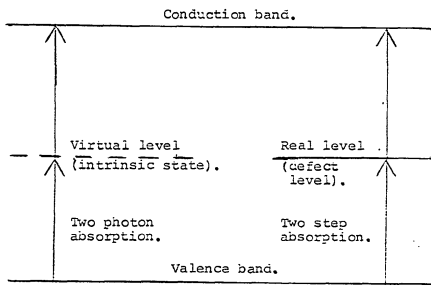

Fig. 4.1.1: Two photon absorption vs two step absorption. Two photon absorption uses a virtual intermediate level, intrinsic to the crystal. Two step absorption uses a real intermediate level, which is a defect state.

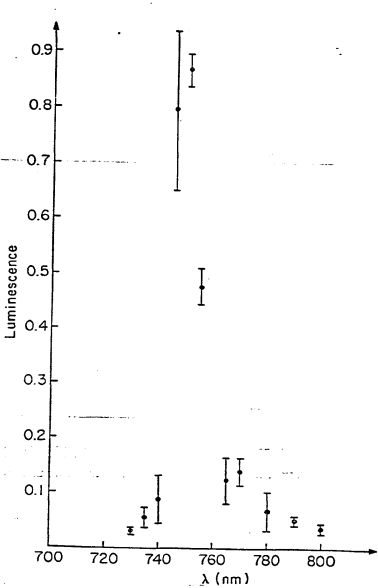

Fig. 4.2.1: Spectrum of anti-Stokes PL at room temperature for SI CdSe(sample H_3).

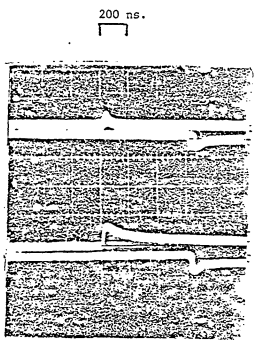

Fig. 4.2.2: Oscilloscope traces showing the room temperature PL at 745 nm for two samples of CdSe, and the intensities of the 1060 nm excitation pulses. The PL from the SI CdSe($> 10^8 \Omega$-cm) had a decay time of less than 40 ns, while the PL from the low resistivity CdSe(12 Ω-cm) had a decay time of 200 ns.

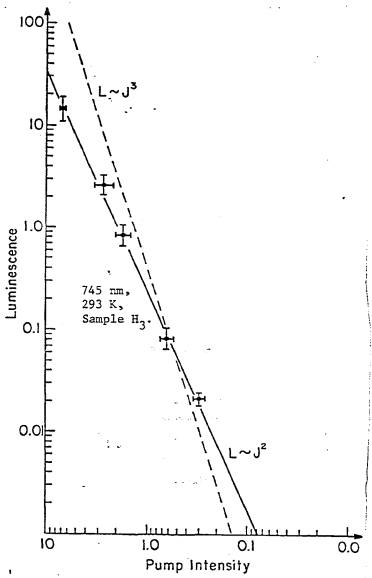

Fig. 4.3.1: Time integrated PL(arbitrary units), at room temperature, as a function of excitation intensity J(arbitrary units). Measured PL(●●) is compared to both a square law(——) and cubic law(---). The PL should vary as a third power of J in the long pulse approximation and as a fourth power of J in the short pulse approximation, for intrinsic two photon absorption.

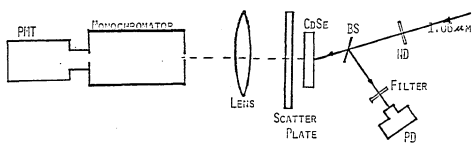

Fig. 4.4.1: Strong pulse transmission experiment. Scatter plate is placed a small distance behind the sample so that part of the transmitted pulse is redirected into the detector, while the direct pulse is measured before the sample. Excitation pulse energy is varied by a neutral density(ND) filter.

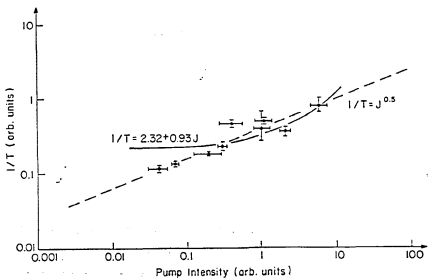

Fig. 4.4.2: Strong pulse transmission(T^{-1}) of a 1.06μm pumping pulse as a function of excitation intensity J. Data points are compared to a least squares fit of $T^{-1}=a+bJ$(——), the two photon absorption formula, and to $T^{-1}=bJ^{0.5}$(---), an empirical formula. The two photon absorption model does not fit well.

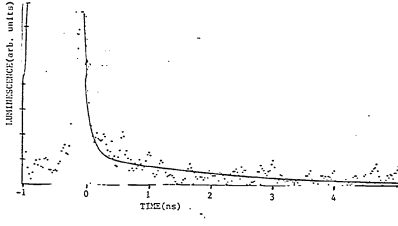

Fig. 4.6.1: Time dependence of PL, at room temperature for sample H_3, measured at 710 nm by a streak camera. The data points were fitted to a bi-exponential curve. The curve shows a short component(~100 ps) which varied with excitation intensity and a long component(2.0 ns) which was independent of excitation intensity.

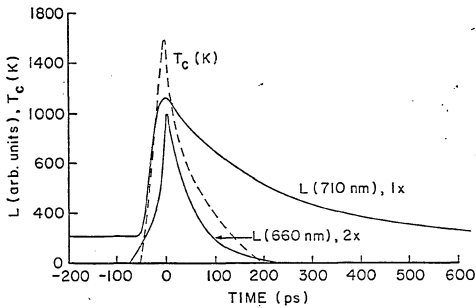

Fig. 4.6.2: Streak camera measurements of PL at 710 nm and 660 nm(——), smoothed for illustration purposes. The carrier temperature T_c(---) is shown as a function of time, where T_c is defined by the formula: $L(660\ nm)/L(710\ nm)=\exp(-\Delta E/k_B T_c)$, $\Delta E=0.132$ eV The carrier temperature T_c has a decay time of 55 ps, and peaks at 1800 K.

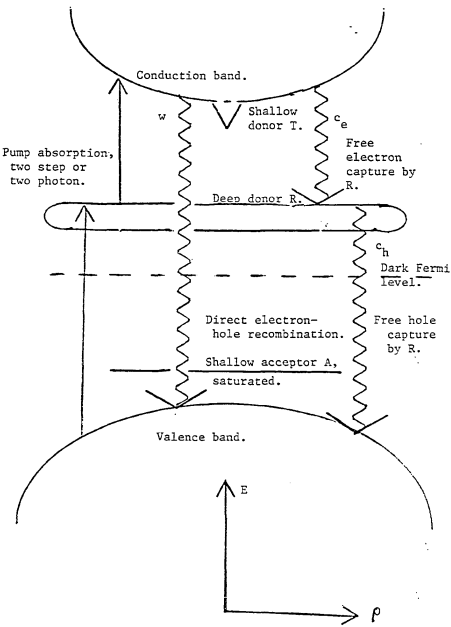

Fig. 4.6.3: Energy level schematic explaining streak camera measurements at the band edge.

TABLE 4.6.1

Bi-exponential fit of the streak camera luminescence using the following equation:

$L(t)=A_F\exp(-t/\tau_F)+A_L\exp(-t/\tau_L)$

where τ_F is for the fast component and τ_L is for the slow component The excitation intensity, J, is in arbitrary units.

Intensity J	λ(nm)	τ_F(ps)	τ_L(ps)	A_F	A_L	A_F/A_L
4.5±0.7	710	105±5	1990±55	156±30	35±5	4.3
1.15±0.21	710	257±18	1975±106	65±12	10±3	6.5
0.53±0.06	710	301±14	1900±100	62±28	13±3	4.7
5.0±0.1	660	71±3	1973±25	33±13	3±1	10.9

Chapter 5

Conclusions and Future Directions

Experiments were performed on undoped, Se vapor annealed SI CdSe using a wide variety of techniques and under various experimental conditions. A new deep level was found and studied. Techniques for characterizing defects in semiconductors were developed.

It was found that the time resolved and nonlinear properties studied in SI CdSe could be explained using three defect bands. First, the main recombination center is a deep level(R), probably a deep donor ≈1.3 eV above the valence band, with a very large cross section for free hole capture. This deep level has degenerate levels and is inhomogenously broadened. Second, a shallow acceptor(A), ≈105 meV above the valence band, is also a recombination center. Third, shallow donors contribute to the band tail luminescence. The shallow donors do not play a major role in the recombination of free carriers in SI CdSe, but are long lived traps in low resistivity CdSe. These three levels cause the picosecond recombination, multi-photon absorption and high electrical resistivity of SI CdSe. Because of the wide range of experimental conditions, different models using the same levels were used to explain the data.

Under low intensity steady state excitation, a two level model by Klasens, using recombination centers R and A, explained the nonlinear PL. A conduction band tail T causes luminescence but was not a recombination center. Different samples can be clas-

sified by different conditions in the Klasens model. The picosecond measurements, both absorption and luminescence, show that R captures holes very rapidly(<10 ps), captures conduction electrons on a nanosecond scale(2 ns at room temperature) and probably transfers electrons to A(≈1 ns at room temperature) by a cascade mechanism. The cascade mechanism is a process where the electron transfers in stages down a ladder of electronic levels by emitting acoustical phonons. The deep level also causes two step absorption and induced dichroism. The induced dichroism shows transfer between degenerate levels within R faster than 10 ps. The deep donor caused optical two step absorption from the valence band to the conduction band. Phenomenological models using these processes explained the results of the picosecond measurements well.

An energy level schematic for SI CdSe which summarizes some of these results is shown in figure 5.1.1. The energy of the defect levels, R and A, are probably accurate. Estimated cross sections and transition rates for nonradiative transitions at room temperature are shown in this figure. These estimates are very rough and their limitations are described in the text. However, this diagram gives a physical insight into the processes by which defects influence the properties of SI CdSe.

This work suggests many future directions. For the material CdSe itself, future work could be done to study the shallow donors in SI CdSe and the dynamics of electrons in LR CdSe. The chemical and physical nature of the defects studied in this thesis, and the effect of the surface on these defects, are still unknown.

First principle calculations were not applied to SI CdSe because the defects were not chemically known. The effect of known dopants, such as Cu, on the temporal and nonlinear properties of CdSe could be compared to first principal theories. Previous studies of the intrinsic properties of CdSe should be reviewed because of the new knowledge of possible effects of uncontrolled defects.

The extrinsic properties of semiconductors under high excitation, especially on a picosecond time scale, should be carefully studied. Measurements on chemically known systems, such as ZnSe:Cu, Si:Au and GaAs:Cr, could be compared to first principle models of atoms in crystal environments. Defects that are generated by growth, annealing, nuclear bombardment or device usage could be detected and characterized by the same techniques used in this thesis. The properties that were shown extrinsic in this thesis, such as picosecond recombination and four wave mixing are important in electronic and optical technology. Therefore, these properties can be altered by suitable doping or bombardment for various device applications.

This thesis also emphasizes the effect unintentional, uncontrolled defects can have on a sample. The use of more than one experimental technique on a single sample, or the use of one technique on more than one sample, could separate the properties of the intrinsic crystal from the properties of the uncontrollable defects.

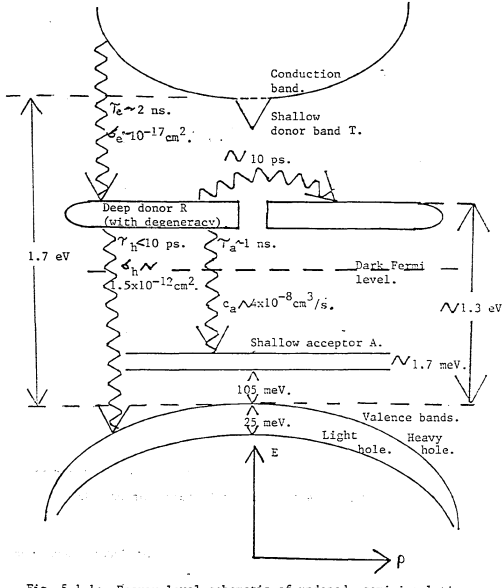

Fig. 5.1.1: Energy level schematic of undoped, semi-insulating CdSe. The major defect level bands are the deep donor, the shallow acceptor and the shallow donor. The parameters of nonradiative transitions of the deep donor are at room temperature.

Appendix A1

a) The coded conditions in the single defect level model by Klasens. The quantities n, p, C, L, I, F and U are defined in chapter 2. Each quantity is shown as a function of excitation intensity U.

Code	a^0	a^+	p	n	C	L	I	F
1111	a	$\frac{U^{\frac{1}{2}}}{\beta^{\frac{1}{2}}}$	$\frac{\gamma U^{\frac{1}{2}}}{\alpha\beta^{\frac{1}{2}}\alpha}$	$\frac{U^{\frac{1}{2}}}{\beta^{\frac{1}{2}}}$	$\frac{\gamma U^{\frac{1}{2}}}{\beta^{\frac{1}{2}}}$	$\frac{\gamma U^{\frac{1}{2}}}{\beta^{\frac{1}{2}}}$	U	$\frac{\delta\gamma U}{\alpha\beta\alpha}$
1112	a	$\frac{U^{\frac{1}{2}}}{\beta^{\frac{1}{2}}}$	$\frac{U}{\alpha a}$	$\frac{U^{\frac{1}{2}}}{\beta^{\frac{1}{2}}}$	U	$\frac{\gamma U^{\frac{1}{2}}}{\beta^{\frac{1}{2}}}$	U	$\frac{\delta U^{\frac{1}{2}}}{\alpha\beta^{\frac{1}{2}}\alpha}$
1121	a	$\frac{\alpha^{\frac{1}{2}}\alpha^{\frac{1}{2}}U^{\frac{1}{2}}}{\delta^{\frac{1}{2}}\alpha^{\frac{1}{2}}\alpha^{\frac{1}{2}}}$	$\frac{\gamma^{\frac{1}{2}}U^{\frac{1}{2}}}{\delta^{\frac{1}{2}}\alpha^{\frac{1}{2}}\alpha^{\frac{1}{2}}}$	$\frac{\alpha^{\frac{1}{2}}\alpha^{\frac{1}{2}}U^{\frac{1}{2}}}{\delta^{\frac{1}{2}}\gamma^{\frac{1}{2}}}$	$\frac{\gamma^{\frac{1}{2}}\alpha^{\frac{1}{2}}\alpha^{\frac{1}{2}}U^{\frac{1}{2}}}{\delta^{\frac{1}{2}}}$	$\frac{\gamma^{\frac{1}{2}}\alpha^{\frac{1}{2}}\alpha^{\frac{1}{2}}U^{\frac{1}{2}}}{\delta^{\frac{1}{2}}}$	$\frac{\alpha\beta\alpha U}{\delta\gamma}$	U
1122	a	$\frac{\alpha^{\frac{1}{2}}\alpha^{\frac{1}{2}}U^{\frac{1}{2}}}{\delta^{\frac{1}{2}}\beta^{\frac{1}{2}}}$	$\frac{\beta^{\frac{1}{2}}U^{\frac{1}{2}}}{\delta^{\frac{1}{2}}\alpha^{\frac{1}{2}}\alpha^{\frac{1}{2}}}$	$\frac{\alpha^{\frac{1}{2}}\alpha^{\frac{1}{2}}U^{\frac{1}{2}}}{\delta^{\frac{1}{2}}\beta^{\frac{1}{2}}}$	$\frac{\beta^{\frac{1}{2}}\alpha^{\frac{1}{2}}\alpha^{\frac{1}{2}}U^{\frac{1}{2}}}{\delta^{\frac{1}{2}}\beta^{\frac{1}{2}}}$	$\frac{\gamma\alpha^{\frac{1}{2}}\alpha^{\frac{1}{2}}U^{\frac{1}{2}}}{\delta^{\frac{1}{2}}\beta^{\frac{1}{2}}}$	$\frac{\beta^{\frac{1}{2}}\alpha^{\frac{1}{2}}\alpha^{\frac{1}{2}}U^{\frac{1}{2}}}{\delta^{\frac{1}{2}}}$	U
1211	a	$\frac{\alpha^{\frac{1}{2}}\alpha^{\frac{1}{2}}U^{\frac{1}{2}}}{\beta^{\frac{1}{2}}\gamma^{\frac{1}{2}}}$	$\frac{\gamma^{\frac{1}{2}}U^{\frac{1}{2}}}{\alpha^{\frac{1}{2}}\beta^{\frac{1}{2}}\alpha^{\frac{1}{2}}}$	$\frac{\gamma^{\frac{1}{2}}U^{\frac{1}{2}}}{\alpha^{\frac{1}{2}}\beta^{\frac{1}{2}}\alpha^{\frac{1}{2}}}$	$\frac{\gamma^{\frac{1}{2}}\alpha^{\frac{1}{2}}\alpha^{\frac{1}{2}}U^{\frac{1}{2}}}{\beta^{\frac{1}{2}}}$	$\frac{\gamma^{\frac{1}{2}}\alpha^{\frac{1}{2}}\alpha^{\frac{1}{2}}U^{\frac{1}{2}}}{\beta^{\frac{1}{2}}}$	U	$\frac{\delta\gamma U}{\alpha\beta\alpha}$
1212	a	$\frac{\alpha\alpha}{\beta}$	$\frac{U}{\alpha\alpha}$	$\frac{U}{\alpha\alpha}$	U	$\frac{\alpha\gamma\alpha}{\beta}$	U	$\frac{\delta U^{\frac{1}{2}}}{x^{\frac{1}{2}}\alpha^{\frac{1}{2}}}$
1221	a	$\frac{\alpha\alpha U^{\frac{1}{2}}}{\gamma\delta^{\frac{1}{2}}}$	$\frac{U^{\frac{1}{2}}}{\delta^{\frac{1}{2}}}$	$\frac{U^{\frac{1}{2}}}{\delta^{\frac{1}{2}}}$	$\frac{\alpha\alpha U^{\frac{1}{2}}}{\delta^{\frac{1}{2}}}$	$\frac{\alpha\alpha U^{\frac{1}{2}}}{\delta^{\frac{1}{2}}}$	$\frac{\alpha\beta\alpha U}{\delta\gamma}$	U
1222	a	$\frac{\alpha\alpha}{\beta}$	$\frac{U^{\frac{1}{2}}}{\delta^{\frac{1}{2}}}$	$\frac{U^{\frac{1}{2}}}{\delta^{\frac{1}{2}}}$	$\frac{\alpha\alpha U^{\frac{1}{2}}}{\delta^{\frac{1}{2}}}$	$\frac{\gamma\alpha\alpha}{\beta}$	$\frac{\alpha\alpha U^{\frac{1}{2}}}{\delta^{\frac{1}{2}}}$	U
2111	$pa^0=\frac{\gamma\alpha}{\alpha}$	a	indefinite	a	γa	γa	βa^0	indefinite
2112	$pa^0=\frac{\beta a^0}{\alpha}$	a	indefinite	a	βa^0	γa	βa^0	indefinite
2121	$\frac{\delta\gamma a^0}{\alpha U}$	a	$\frac{U}{\delta a}$	a	γa	γa	βa^0	U
2122	$\frac{\delta\beta a^0}{\alpha U}$	a	$\frac{U}{\delta a}$	a	βa^0	γa	βa^0	U
2211	$\frac{\gamma\beta a^0}{\alpha U}$	a	$\frac{U}{\beta a}$	$\frac{U}{\beta a}$	γa	γa	U	$\frac{\delta U^{\frac{1}{2}}}{\beta^{\frac{1}{2}}a^{\frac{1}{2}}}$
2212	$\frac{\beta a}{\alpha}$	a	$\frac{U}{\beta a}$	$\frac{U}{\beta a}$	U	γa	U	$\frac{\delta U^{\frac{1}{2}}}{\beta^{\frac{1}{2}}a^{\frac{1}{2}}}$
2221	$\frac{\delta^{\frac{1}{2}}\gamma a}{\alpha U^{\frac{1}{2}}}$	a	$\frac{U^{\frac{1}{2}}}{\delta^{\frac{1}{2}}}$	$\frac{U^{\frac{1}{2}}}{\delta^{\frac{1}{2}}}$	γa	γa	$\frac{\beta\alpha U^{\frac{1}{2}}}{\delta^{\frac{1}{2}}}$	U
2222	$\frac{\beta a}{\alpha}$	a	$\frac{U^{\frac{1}{2}}}{\delta^{\frac{1}{2}}}$	$\frac{U^{\frac{1}{2}}}{\delta^{\frac{1}{2}}}$	$\frac{\beta\alpha U^{\frac{1}{2}}}{\delta^{\frac{1}{2}}}$	γa	$\frac{\beta\alpha U^{\frac{1}{2}}}{\delta^{\frac{1}{2}}}$	U

b) Code for different conditions of the single defect model. One digit is chosen from each column.

(1) $a=a^0$	(1) $n=a^+$	(1) U=I	(1) C=L
(2) $a=a^+$	(2) n=p	(2) U=I	(2) C=I

Appendix A2

Transition intensities (i.e., breaking points) for the single defect level model by Klasens. When the excitation intensity U passes a transition intensity U_i, the coded condition and the values of m change.

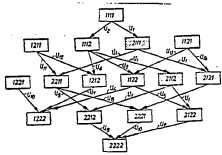

$$U_1=\beta a^2;\ U_2=\frac{\gamma^2}{\beta};\ U_3=\frac{\alpha^2\beta a^2}{\delta^2};\ U_4=\frac{\alpha^2 a^2}{\beta};$$

$$U_5=\frac{\beta\delta a^2}{\alpha};\ U_6=\frac{\alpha^2\delta a^2}{\beta^2};\ U_7=\delta a^2;\ U_8=\frac{\beta^2 a^2}{\delta}$$

$$U_9=\gamma a;\ U_{10}=\frac{\delta\gamma^2}{\beta^2};\ U_{11}=\frac{\beta\gamma a}{\alpha};\ U_{12}=\frac{\alpha\gamma a}{\beta};$$

$$U_{13}=\frac{\delta\gamma^3}{\alpha\beta^2 a};\ U_{14}=\frac{\delta\gamma a}{\alpha}.$$

Appendix A3

a) The coded conditions in the two defect level model by Klasens. The quantities n, p, I and R are defined in chapter 2. The value of m, the value of the exponent for the excitation intensity U, is shown for each quantity.

Code	n	p	I	R	Code	n	p	I	R
111111	½	½	1	1	113111	½	½	1	1
111112	½	½	1	½	113112	½	½	1	½
111121	½	1	1	½	113121	1	1	1	2
111122	1	1	1	1	113122	2	1	1	2
111211	½	½	1	1	113211	½	½	1	1
111212	1	½	½	1	113212	1	½	½	1
111221	½	1	1	1	113221	½	½	½	1
111222	1	1	1	1	113222	1	½	½	1
112111	½	½	1	½	114111	½	½	1	1
112112	½	½	1	½	114112	½	½	1	½
112121	½	1	1	½	114121	1	1	1	2
112122	1	1	1	1	114122	1	1	1	1
112211	½	½	1	1	114211	½	½	1	1
112212	1	1	2	1	114212	1	1	2	1
112221	½	½	1	1	114221	½	½	½	1
112222	1	2	2	1	114222	1	1	1	1
121111	1	0	1	0	123111	1	0	1	0
121112	1	0	1	0	123112	1	0	1	0
121121	1	1	1	1	123121	1	0	0	0
121122	1	1	1	1	123122	1	0	0	0
121211	∞	0	∞	0	123211	∞	0	∞	0
121212	∞	0	∞	0	123212	∞	0	∞	0
121221	1	1	1	1	123221	∞	0	∞	0
121222	1	1	1	1	123222	∞	0	∞	0
122111	½	½	1	½	124111	½	½	1	½
122112	½	½	1	½	124112	½	½	1	½
122121	1	1	1	1	124121	1	1	1	1
122122	1	1	1	1	124122	1	1	1	1
122211	1	1	2	1	124211	1	1	2	1
122212	1	1	2	1	124212	1	1	2	1
122221	1	1	1	1	124221	1	1	1	1
122222	1	1	1	1	124222	1	1	1	1

Continued on the next page.

Appendix A3 a) Continued from the previous page

Code	n	p	I	R	Code	n	p	I	R
211111	0	∞	0	∞	221111	1	1	1	1
211112	1	1	1	1	221112	1	½	1	½
211121	0	∞	0	∞	221121	1	2	1	2
211122	1	1	1	1	221122	1	1	1	1
211211	0	1	0	1	221211	1	1	1	1
211212	1	1	1	1	221212	2	1	2	1
211221	0	1	0	1	221221	½	1	½	1
211222	1	1	1	1	221222	1	1	1	1
212111	0	∞	0	∞	222111	0	∞	0	∞
212112	0	∞	0	0	222112	0	∞	0	∞
212121	0	∞	0	∞	222121	0	∞	0	∞
212122	0	∞	0	0	222122	0	∞	0	∞
212211	0	1	0	1	222211	0	1	0	1
212212	0	∞	0	0	222212	0	1	0	1
212221	0	1	0	1	222221	0	1	0	1
212222	0	∞	0	0	222222	0	1	0	1
213111	1	1	1	2	223111	1	0	1	0
213112	1	½	1	1	223112	1	0	1	0
213121	1	1	1	2	223121	1	0	1	0
213122	1	½	1	1	223122	1	0	1	0
213211	½	1	½	1	223211	∞	0	∞	0
213212	1	½	1	1	223212	∞	0	∞	0
213221	½	½	½	1	223221	∞	0	∞	0
213222	1	½	1	1	223222	∞	0	∞	0
214111	1	1	1	2	224111	1	1	1	1
214112	1	1	1	1	224112	1	1	1	1
214121	1	1	1	2	224121	1	1	1	1
214122	1	1	1	1	224122	1	1	1	1
214211	½	½	½	1	224211	1	1	1	1
214212	1	1	1	1	224212	1	1	1	1
214221	½	½	½	1	224221	1	1	1	1
214222	1	1	1	1	224222	1	1	1	1

b) Code for different conditions in the two defect level model. One digit is chosen from each row.

(1) $a=a_0^0$ (2) $a=a_-^+$

(1) $h=h_0^0$ (2) $h=h_-^+$

(1) $a^+=h^-$ (2) $a^-=n$ (3) $h^-=p$ (4) $n=p$

(1) U=I (2) U=R

(1) C=L (2) C=I

(1) E=B (2) E=R

Appendix A4

Partial list of transition intensities (i.e., breaking points) for the two defect level model by Klasens. When the excitation intensity U passes a transition intensity U_i, the coded condition and the values of m change.

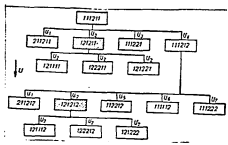

$$U_1 = \frac{\eta\gamma a}{\alpha};\quad U_2 = \frac{\eta\gamma h^2}{a\alpha};\quad U_3 = \frac{\gamma^2\eta^2 h^2}{\alpha\beta^2\zeta^2 a}$$

$$U_4 = \frac{\zeta^2 a a}{\eta\gamma};\quad U_5 = \frac{\alpha\epsilon^2 a h^2}{\eta\gamma};\quad U_6 = \frac{\epsilon^2\eta\gamma h^2}{\beta^2 a a};$$

$$U_7 = \frac{\epsilon\gamma h}{\beta}.$$

Appendix B1

Program DONOR.R, for calculating the concentrations of electrons in the deep level and the free holes as a function of time. Rate equations enter the program by subroutine EQNS.R, are solved by library function ODES and placed in files by subroutine PRINT.R. Transmission as a function of time is then calculated by TRNS.R.

```
external eqns,print
common nufq,nuaq,cf,ca,tp
real x(2),errpar(2),nufq,nuaq,cf,ca,tp
open(1,file="rr.dat")
open(2,file="pr.dat")
open(3,file="rosen.dat")
write(6,1)1 format(" enter nufq, nuaq, cf, ca, tp")
read(5,2)nufq,nuaq,cf,ca,tp2 format(5g14.7)
write(3,3)nufq,nuaq,cf,ca,tp3 format(" nufq=nuaq,cf,ca,tp",5(" ",g14.7))
write(6,4)4 format(" enter errpar(1), errpar(2)")
read(5,5) errpar(1),errpar(2)5 format(2g14.7)
write(3,6)errpar(1),errpar(2)6 format(" errpar = ",2g14.7)
tstart=-20.
tstop=1390.
dt=1
x(1)=0.
x(2)=0.
call odes(eqns,x,2,tstart,tstop,dt,errpar,print)
close(1)
close(2)
close(3)
stop
end
```

Appendix B2

Program EQNS.R, containing the rate equations for the concentration of deep donor electrons. The rate equations used are described in the text(equation 3.5.1).

```
      subroutine eqns(t,x,n,rhs)
      common mufc,muaq,cf,ca,to
      dimension rhs(2),x(2)
      real mufc,muaq,cf,ca,to
      rhs(1)=(mufc+muaq)*exp(-(t/to)**2)-cf*x(1)*x(2)-ca*x(1)*(x(1)-x(2))
      rhs(2)=mufc*exp(-(t/to)**2)-cf*x(1)*x(2)
      return
      end
```

Appendix B3

Program PRINT.R, which makes files for the deep donor electrons, the free holes and a display table for both.

```
subroutine print(t0,x0,t1,x1,nact,tatmax)
real x0(2),x1(2),e(2)
if(t0==t1)return
write(1,1)t1,x1(1): 1 format(2(' ',1pE14.7))
write(2,2)t1,x1(2)
write(3,3)t1,x1(1),x1(2): 3 format(' t, nrs of x3(' ',1pE14.7))
return
end
```

Appendix B4

Program TRNS.R, which calculates the transmission as a function of time from the deep donor concentration(using equation 3.5.2) and produces a file for plotting.

```
c@se@d abcr,x
real abcr,x(1002,2)
open(1,file='xr.dat')
open(2,file='trans.dat')
write (6,1)1 format('enter absorption cross section')
read(5,2)abcr;2 format(g14.7)
jt=1
3 read(1,3,end=14)x(jt,1),x(jt,2);3 format(2g14.7)
x(jt,2)=exp(-abcr*x(jt,2))
write(2,3)x(jt,1),x(jt,2)
jt = jt+1
go to 3
14 write(6,4);4 format('transmission is now in trans.dat')
close(1)
close(2)
stop
end
```

BIBLIOGRAPHY

(1) R. A. Abram, Philisophical Magazine B**46**, 13(1982).

(2) R. R. Alfano and S. L. Shapiro, Scientific American **6**, 46(1973).

(3) R. R. Alfano, ed. Semiconductors Probed by Ultrafast Laser Spectroscopy V.2, (Academic Press, N.Y.)1984.

(4) D. H. Auston, A. M. Glass and A. A. Ballman, Phys. Rev. Lett.**28**, 897(1972).

(5) J. L. Ayral, J. P. Pocholle, J. Raffy and M. Papuchon, Optics Comm. **49**, 405(1984).

(6) J. H. Bechtel and W. L. Smith, Phys. Rev. B**13**, 3515(1976).

(7) M. F. Becker, R. M. Walser, J. G. Ambrose and D. Y. Sheng, "Picosecond, 1.06 μm Laser-Induced Amorphous Phases in Thin, Single Crystal Silicon Membranes", Picosecond Phenomena III(Springer-Verlag, N.Y.)1980.

(8) G. L. Belen'kii, A. V. Lyubchenko and M. K. Sheinkman, Sov. Phys. Semi. **2**, 445(1968).

(9) J. L. Birman, Proceedings of the International Conference on Luminescence, Budapest, Hungary, 1966(unpublished).

(10) J. L. Birman, J. Electrochem. Soc. **107**, 409(1960).

(11) G. A. Bocko, V. S. Dneprovski and W. Sibbet, Phys. Stat. Sol. **85**, 111(1978).

(12) W. L. Bond, J. Appl. Phys. **35**, 539(1964).

(13) J. Bourgoin and M. Lanoo, Point Defects in Semiconductors II, (Springer-Verlag, Berlin)1983.

(14) R. Braunstein and N. Ockman, Phys. Rev. A**134**, 499(1964).

(14) R. Braunstein and N. Ockman, Phys. Rev. A134, 499(1964).

(15) S. F. Bryant, V.S. Dneprovski and W. Sibbet, App. Phys. Lett. 33, 863(1978).

(16) R. H. Bube, H. E. Macdonald and J. Blanc, J. Phys. Chem. Solids 22, 173(1961).

(17) Felix Cardon and R. H. Bube, J. App. Phys. 35, 7344(1964).

(18) T. Y. Chang, Opt. Engineering 20, 220(1981).

(19) M. Foresti, private communication.

(20) A. B. Fowler, J. Phys. Chem. Solids 22, 181(1961).

(21) S. Guha, E. W. van Stryland and M. J. Soileau, Opt. Lett. 10, 285(1985).

(22) R. E. Halsted, E. F. Apple and J. S. Prener, Phys. Rev. Lett. 2, 420(1959).

(23) H. Hatano, Y. Kokubun,H. Watanabe and M. Wada, Jap. J. Applied Phys.18, 539(1979).

(24) D. M. Heinz and E. Banks,J. Chem. Phys. 24, 391(1956).

(25) C. H. Henry and D. V. Lang, Phys. Rev. B15, 989(1977).

(26) P. P. Ho and R. R. Alfano, Phys. Rev. A20, 2170 (1979).

(27) Ming-Pan Hung, Nobumitan Thashi and Kenzo Igaki, Jap. J. App. Phys.8, 652(1969).

(28) D. H. Huppert, Z. Harzion and and S. Gottefeld,"Time Resolved Photoluminescence Study in n-type CdS and CdSe Photoelectrode",Picosecond Phenomena Conference III(Springer Verlag,N.Y.)1972.

(29) M. Junnakar, private communication.

(30) H. A. Klasens, Nature 158, 306(1946).

(31) H. A. Klasens, J. Phys. Chem. Solids 7, 175(1958).

38, 60(1948).

(33) A. Kobayashi, O. E. Sankey and J. D. Dow, Phys. Rev. B28, 946(1983).

(34) H. Kuroda and Shionoya, J. Phys. Soc. of Jap. **36**, 476(1974).

(35) H. Kuroda and S. Shionoya, J. of Luminescence **24**, 601(1981).

(36) P. T. Landsberg and A. R. Beattie, J. Phys. Chem. Sol. 8, 73(1959).

(37) M. Lax, J. Phys. Chem. Solids 8, 66(1959).

(38) D. von der Linde, D. H. Auston, A. M. Glass and K. M. Rodgers, Solid State Communication **14**, 137(1974).

(39) R. L. Longini and R. F. Greene, Phys. Rev. **102**, 992(1956).

(40) G. Mandel, Phys. Rev. **134**, A1073(1964).

(41) G. M. Martin, Appl. Phys. Lett. **39**, 747(1981).

(42) A. Migus, J. L. Martin, R. Astier, A. Antonetti, D. Hulin and A. Mysyrowicz,"Picosecond Time-Resolved Resonant Two-Photon Absorption in Cu_2O",Picosecond Phenomena Conference II(Springer-Verlag, N. Y.)1980.

(43) A. Mitonneau and A. Mircea, Sol. Stat. Comm. **30**, 157(1979).

(44) G. G. Neumark and K. Kosa,"Deep Levels in Wide Gap III-V Semiconductors", Semiconductors and Semimetals XIX, ed. R. K. Richardson and A. C. Beer(Academic Press, 1983).

(45) N. Ockman and D. Dorsinville, to be published.

(46) J. I. Pankove, Optical Properties in Semiconductors, (Dover, N.Y.)1971.

(47) E. Yu Perlin, Opt. Spectrosc. (USSR) **50**, 387 (1981).

(48) John F. Reintjes and James C. McGroddy, Phys. Rev. Letts. **30**, 901(1973).

901(1973).

(49) J. F. Reintjes, J. C. McGroddy and A. E. Blakeslee, J. of App. Phys. **46**, 879(1975).

(50) A. Rose, Concepts in Photoconductivity and Allied Processes(Interscience, New York)1963.

(51) D. L. Rosen, Q. X. Li and R. R. Alfano, Phys. Rev. B**31**, 2396(1985).

(52) Jagdeep Shah, Phys. Rev. B**9**, 562(1974).

(53) N. Schiller, M. Grant and R. R. Alfano, Phys. Teacher **10**, 396(1977).

(54) N. H. Schiller and R. R. Alfano, Laser Focus 8, 43(1982).

(55) A. Starosin and V. V. Serdyuk, Sov. Phys. Semicond. **9**, 297(1975).

(56) I. A. Starosin and B. S. Vakarov, Sov. Phys. Semicond. 14, 1325(1980).

(57) A. F. Stewart and M. Basa, App. Phys. Lett. 37, 1040(1980).

(58) G. B. Stringfellow and R. H. Bube, Phys. Rev. **171**, 903(1968).

(59) M. D. Sturge, Phys. Rev. 127, 768(1962).

(60) I. E. Ture, F. Poulin, A. W. Brinkman and J. Woods, Phys. Stat. Sol.(a) 77, 535(1983).

(61) D. Waldeck, A. J. Cross, D. B. Macdonald and G. R. Fleming, J. Chem. Phys. **74**, 3381(1981).

(62) M. E. Wise and H. A. Klasens, J. Opt. Soc. Am. 38, 226(1948)

(63) N. I. Vitrikhovsky, L. F. Gudimenho, O. P. Maznichenko, V. N. Malinko, E. V. Pidlisnii and S. F. Terekhova, Ukr. Fiz. Zh.(Russ. Ed.) **12**, 796(1967).

(64) A. Yariv and P. Yeh, Optical Waves in Crystals, (Wiley,

N.Y.)1984.

(65) H. Yoshida, H. Saho, and S .Shionoya, J. Phys. Soc. Jpn. 40, 881(1981).

(66) H. Yoshida and S. Shionoya, J. of Luminescence **24**, 601(1981).

(67) Yu. Yu. Vaitkus and Yu. K. Vishchakas, Sov. Phys. Semi. 1, 1462(1968).

(68) V. A. Zyul'kov, V. P. Gribkovskii, V. A. Ivanov and M. A. Katibnikov, Sov. Phys. Semicond. **17**, 1211(1983).